



UNIVERSIDAD DE CHILE  
FACULTAD DE CIENCIAS FÍSICAS Y MATEMÁTICAS  
DEPARTAMENTO DE FÍSICA

## ELECTRON HEATING IN A COLLISIONLESS PLASMA

TESIS PARA OPTAR AL GRADO DE  
MAGÍSTER EN CIENCIAS, MENCIÓN FÍSICA

ASTOR EMAR SANDOVAL PARRA

PROFESOR GUÍA:  
MARIO RIQUELME HERNÁNDEZ

MIEMBROS DE LA COMISIÓN:  
WALTER MAX-MOERBECK ASTUDILLO  
PABLO MOYA FUENTES  
ANDREAS REISENEGGER VON OEPEN

SANTIAGO DE CHILE  
2019

RESUMEN DE LA MEMORIA PARA OPTAR  
AL TÍTULO DE MAGÍSTER EN CIENCIAS, MENCIÓN FÍSICA  
POR: ASTOR EMAR SANDOVAL PARRA  
FECHA: 2019  
PROF. GUÍA: MARIO RIQUELME HERNÁNDEZ

## ELECTRON HEATING IN A COLLISIONLESS PLASMA

Los plasmas son comunes en diferentes sistemas astronómicos. Una parte importante de estos plasmas están en el régimen no colisional, en que el camino libre medio de las partículas que lo componen es más grande que el tamaño del sistema. Un ejemplo de este tipo de objetos es el disco de acreción que se encuentra en las cercanías del agujero negro ubicado en el centro de la Vía Láctea, Sagitario A\* (Sgr A\*). Por su baja colisionalidad, se espera que el plasma en Sgr A\* no siga una distribución de Maxwell-Boltzmann. Además, por la mayor eficiencia radiativa de los electrones, es también esperable que estos tengan menor temperatura que los iones.

El grado en que se calientan los electrones en un sistema no colisional, así como su espectro de energía, tienen importantes consecuencias observacionales. Existen diversos mecanismos que pueden transferir energía a los electrones. Entre ellos están: reconexión magnética, interacción onda-partícula, y viscosidad anisotrópica. En esta tesis nos enfocamos en el calentamiento de electrones por medio de la interacción onda partícula y por calentamiento viscoso. Para ello realizamos simulaciones “particle-in-cell” (o PIC) de un plasma no colisional, magnetizado y sujeto a un cizalle permanente. Este cizalle produce una amplificación del campo magnético, obteniéndose así una anisotropía de presión en las partículas, debido a la invarianza adiabática de su momento magnético. Esta anisotropía produce inestabilidades cinéticas en el plasma, las que propagan ondas en escalas del radio de Larmor de las partículas. Algunos ejemplos relevantes para nuestro estudio son las inestabilidades de whistler e ion-ciclotrón. Estas inestabilidades pueden resonar preferentemente con los electrones e iones, respectivamente, otorgando o quitando energía a las partículas.

Realizamos simulaciones con moderadas razones de masa entre iones y electrones, para estudiar a los electrones en el régimen cinético. Consideramos consistentemente el régimen no-lineal y cuasi-estacionario de las inestabilidades. Estudiamos el calentamiento de los electrones, y se encontró que estos se calientan principalmente por viscosidad. Sin embargo, se encontró un calentamiento extra, el que es transferido desde los iones a los electrones debido a la interacción de estos últimos con las ondas ion-ciclotrón (las que a su vez son principalmente producidas por los iones). Este calentamiento extra aumenta con la magnetización y disminuye al aumentar la razón de masa y la temperatura de los iones. Además, la componente no térmica del espectro de energía de los electrones se ve fuertemente modificada cuando el radio de Larmor de estos es similar al de los iones. Esta componente no térmica se asemeja bastante a lo que se infiere de observaciones de sistemas como Sgr A\*. Nuestro trabajo nos permitió entonces encontrar condiciones que facilitan el calentamiento y aceleración no térmica de electrones debido a la transferencia de energía entre iones y electrones en plasmas no colisionales.

THESIS ABSTRACT

FOR THE DEGREE OF: MAGÍSTER EN CIENCIAS, MENCIÓN FÍSICA

CANDIDATE: ASTOR EMAR SANDOVAL PARRA

DATE: 2019

THESIS ADVISOR: MARIO RIQUELME HERNÁNDEZ

## **ELECTRON HEATING IN A COLLISIONLESS PLASMA**

Plasmas are common in different astronomical systems. An important part of these plasmas are in the collisionless regime, in which the mean free path of the particles is larger than the size of the system. An example of this type of plasma is the accretion disk near the black hole at the center of the Milky Way, Sagittarius A\* (Sgr A\*). Because of its low collisionality, it is expected that the plasma in Sgr A\* will not follow a Maxwell-Boltzmann distribution. In addition, due to their high radiative efficiency of the electrons, the electron temperature is expected to be smaller than the one of the ions.

The efficiency of electron heating in a collisionless system, as well as their resulting energy spectrum, have important observational consequences. There are several mechanisms that can transfer energy to electrons. Among them are: magnetic reconnection, wave-particle interaction, and anisotropic viscosity. In this thesis, we focus on the heating of electrons by wave-particle interaction and by anisotropic viscosity. To do this we perform particle-in-cell (or PIC) simulations of a collisionless plasma, magnetized and subject to a permanent shear. This shear produces an amplification of the magnetic field, thus causing the growth of a pressure anisotropy, due to the adiabatic invariance of the particles' magnetic moment.. This anisotropy produces kinetic instabilities in the plasma, which propagate waves on scales of the Larmor radius of the particles. Some relevant examples for our study are the whistler and ion-cyclotron instabilities. These instabilities can resonate preferentially with electrons and ions, respectively, giving or taking energy away from the particles.

We perform simulations with moderate mass ratios between ions and electrons to study electrons in the kinetic regime. Our simulations consistently capture the non-linear and quasi-stationary regime of instabilities. We studied the heating of electrons, and found that electrons are heated mainly by viscosity. However, extra heating was found, which is transferred from the ions to the electrons due to the interaction of the latter with the ion-cyclotron waves (which in turn are mainly produced by the ions). This extra heating increases with magnetization and decreases as the mass ratio and ion temperature increase. In addition, the non-thermal component of the electron energy spectrum is strongly modified when the Larmor radius of the electrons is similar to that of the ions. This non-thermal component is quite similar to what is inferred from observations of systems like Sgr A\*. Our work thus allowed us to find conditions that ease the non-thermal heating and acceleration of electrons due to the transfer of energy between ions and electrons in collisionless plasmas.

# Agradecimientos

Powered@NLHPC: Esta tesis fue parcialmente apoyada por la infraestructura de supercómputo del NLHPC (ECM-02)

# Contents

|   |              |
|---|--------------|
| <b>Introduction</b>                                   | <b>1</b>     |
| <b>1 The physical situation and simulation setup</b>  | <b>6</b>     |
| 1.1 The physical situation . . . . .                  | 6            |
| 1.2 Simulation setup . . . . .                        | 7            |
| <b>2 Suitability of the 1D approach</b>               | <b>10</b>    |
| 2.1 Comparing 1D and 2D simulations . . . . .         | 10           |
| 2.2 Fourier Analysis . . . . .                        | 14           |
| <b>3 Results</b>                                      | <b>18</b>    |
| 3.1 Electron Heating Rate . . . . .                   | 18           |
| 3.2 Electron acceleration . . . . .                   | 27           |
| 3.3 Discussion . . . . .                              | 30           |
| <b>Conclusion</b>                                     | <b>33</b>    |
| <b>Bibliography</b>                                   | <b>36</b>    |
| <b>A The Chew-Goldberg-Low Equation of State</b>      | <b>I</b>     |
| A.1 The First Adiabatic Invariant . . . . .           | II           |
| A.2 The Second Adiabatic Invariant . . . . .          | III          |
| A.3 Equation of state . . . . .                       | IV           |
| <b>B Lack of collision between electrons and ions</b> | <b>VI</b>    |
| <b>C Magnetic Amplification</b>                       | <b>IX</b>    |
| <b>D Viscous heating</b>                              | <b>XI</b>    |
| <b>E Second-order Fermi acceleration</b>              | <b>XIII</b>  |
| <b>F Magnetic Reconnection</b>                        | <b>XVI</b>   |
| F.1 The Sweet–Parker model . . . . .                  | XVII         |
| <b>G The Code</b>                                     | <b>XVIII</b> |
| G.1 The algorithm of a PIC code . . . . .             | XX           |
| G.1.1 Step 1: Pushing particles . . . . .             | XX           |

|          |  |             |
|----------|--|-------------|
| G.1.2    | Step 2: Current deposition . . . . .           | XX          |
| G.1.3    | Step 3: Evolution of the fields . . . . .      | XXI         |
| G.2      | Boundary conditions . . . . .                  | XXIII       |
| G.2.1    | Particles . . . . .                            | XXIII       |
| G.2.2    | Fields . . . . .                               | XXIII       |
| <b>H</b> | <b>One Dimensional simulations</b>             | <b>XXIV</b> |
| H.1      | Evolution of $\vec{E}$ and $\vec{B}$ . . . . . | XXV         |
| H.2      | Particles evolution . . . . .                  | XXVI        |

# List of Tables

|     |   |   |
|-----|---|---|
| 1.1 | Set of simulations performed in this thesis . . . . . | 9 |
|-----|---|---|

# List of Figures

|     |  |      |
|-----|--|------|
| 1.1 | Sketch of our simulation domain . . . . .  | 7    |
| 2.1 | Fluctuations in the magnetic field . . . . .   | 12   |
| 2.2 | Comparison between simulations in one and two dimensions . . . . .   | 13   |
| 2.3 | Dispersion relation . . . . .  | 16   |
| 2.4 | Evolution of the energy contained in the fluctuations of the magnetic field . .                                  | 17   |
| 3.1 | Electron heating rate, and energy density in magnetic fluctuations. . . . .                                      | 20   |
| 3.2 | Particles heating rate, and energy density in magnetic fluctuations. . . . .                                     | 22   |
| 3.3 | The heating rate of electrons and total plasma with the same temperature of species. . . . .                     | 24   |
| 3.4 | The heating rate of electrons and total plasma with hot ions. . . . .  | 25   |
| 3.5 | Energy density in magnetic fluctuations for different temperature ratios . . .                                   | 26   |
| 3.6 | Electron energy distribution . . . . .   | 28   |
| 3.7 | Comparison of electron spectra, for ions with different masses and at the same temperature as electrons. . . . . | 29   |
| 3.8 | Comparison of electron spectra, for ions with different masses and at the same temperature as electrons. . . . . | 29   |
| 3.9 | Power spectrum of magnetic field fluctuation. . . . .  | 31   |
| A.1 | The three types of motion for a particle trapped in an axially symmetric magnetic mirror field . . . . .         | II   |
| A.2 | The coordinate system used for analyzing the motion of a charged particle in a magnetic mirror field. . . . .    | III  |
| E.1 | Schematic picture of the collision between a charged particle and a magnetic cloud. . . . .                      | XIII |
| F.1 | The magnetic field geometry across planar current sheet. . . . .   | XVI  |
| F.2 | The magnetic field geometry near reconnection region. . . . .  | XVII |
| G.1 | The PIC cycle during a time step $\Delta t$ . . . . .  | XIX  |
| G.2 | A weighting technique to interpolate charges and current . . . . .   | XXI  |
| G.3 | Spatial distribution of the fields discretized proposed by Yee . . . . .   | XXII |

# Introduction

According to the current cosmological paradigm, the Universe is constituted mainly by dark matter, which at the moment has been impossible to observe. Dark matter accounts for about 86% of matter content of the Universe, with almost all the remaining 14% of visible matter (normally called “baryonic”) being in the state of a highly ionized plasma. This includes stars, a significant fraction of the gas between stars (called interstellar medium or ISM), and the gas between galaxies (called intergalactic medium or IGM). It is believed that the IGM contains most of the baryonic matter in the Universe, and it is formed by an almost completely ionized plasma [36].

## Non-thermal electrons in Sgr A\*

Various astrophysical systems are expected to have a plasma with very low density and/or very high temperature, which makes the Coulomb collision between particles (ions and electrons) very infrequent. It is believed that this low-collisionality condition has important consequences on the observational properties of these systems. Some examples are: the plasma between galaxies in galaxy clusters (i.e., the intracluster medium or ICM), the solar coronae, stellar and solar winds, and some types of accretions disks.

In this thesis, we will concentrate on the case of a low-collisionality accretion disks. One example of this type of disks is the gas falling onto Sagittarius A\* (Sgr A\*), the supermassive ( $\sim 4 \cdot 10^6 M_\odot$  [23]) black-hole at the center of the Milky Way<sup>1</sup>. Indeed, due to its low density (inferred from its low luminosity), the expected time for particles to share their energy and get thermalized has been estimated to be much larger than the time for the plasma to be accreted onto the black hole  $\tau_{acc}$ . More precisely, at radius  $r \lesssim 10R_s$  (where  $R_s$  is the Schwarzschild radius of the black hole)  $\tau_{acc}$  is much shorter than the time taken by the electrons to reach thermal equilibrium by electron-electron interaction, which is in turn much shorter than the time taken by ions (we will consider that all ions are protons) to reach thermal equilibrium with electrons.

The low collisionality between particles makes the accretion process onto Sgr A\* an intrinsically non-thermal process, which implies that the different species do not have necessarily the same temperatures and that their energy spectra may not correspond to Maxwell-Boltzmann

---

<sup>1</sup>This mass was obtained following the orbits of 28 stars observed with high-resolution, near infrared astrometric techniques, and using velocities obtained from spectra. This information allowed to obtain both the distance to Sgr A\* ( $R_0 \approx 8.3$  kpc) and its mass[23].

distributions. Indeed, the temperatures of electrons ( $T_e$ ) and ions ( $T_i$ ) can be different, with the ions being warmer than the electrons. This can happen for two reasons. First, the gravitational energy is mainly carried by the more massive ions, and the lack of collisions does not allow this energy to be efficiently transferred to the electrons. Second, various radiation processes are expected to occur in these disks, which are more effective in cooling the less massive electrons. Additionally, the time in which the internal energy of the particles grows is shorter than the time needed to reach the thermal equilibrium, opening the possibility for the velocity distributions of the different species to be different from a Maxwell-Boltzmann distribution. This implies that a weakly collisional accretion disk may in principle act as accelerator of non-thermal particles. Although this possibility is interesting both in the cases of ions and electrons, in this thesis we will concentrate on the heating and acceleration of electrons.

The presence of non-thermal electrons in Sgr A\* is also supported by multi-wavelength observations, both in the quiescent and variable (or “flaring”) states of the system. In the quiescent regime, a non-thermal tail component in the electron energy spectrum is typically needed to reproduce a low-frequency radio excess (at frequency  $10^{11}$  Hz). This tail has been estimated to carry a low fraction of the electron energy and it is typically modeled as a power-law with spectral index  $\alpha \sim 3.5$ .<sup>2</sup> The flares that usually appear in the IR and X-ray energies suggest the presence of non-thermal electrons as well, but with a harder tail ( $\alpha \sim 2.4$ ; [40]). There are also magnetohydrodynamic (MHD) simulations of the flaring state of Sgr A\* that support the idea of non-thermal electrons [9]. Indeed [9] studied different electron heating mechanisms, showing that in the absence of non-thermal electrons, the main features of Sgr A\* in its flaring state (e.g., the intensity of the X-ray flares) cannot be reproduced.

These theoretical arguments and observational evidence are the main motivation for this work. This thesis thus deals with the problem of electron heating and acceleration in low-luminosity accretion flows such as the one in Sgr A\*. In what follows we will briefly describe the most relevant physical processes for electron heating and acceleration in these systems. In particular, our work focuses on possible (collisionless) mechanisms for energy transfer between ions and electrons produced by the interaction between particles and plasma waves during the process of “viscous heating” of the plasma.

## Electron heating and acceleration mechanisms

The electron temperature ( $T_e$ ) is one of the most important parameter for calculations of the radiation spectrum near the black hole. In the absence of collisions between electrons and ions  $T_e$  is expected to be different from the ion temperature ( $T_i$ ). As a consequence of the higher radiative efficiency of the electrons, the inequality  $T_e \ll T_i$ , is expected to hold (see Appendix B), but the exact value of  $T_e/T_i$  is unknown.

In weakly collisional accretion disks, the main source of energy for particle heating and accel-

---

<sup>2</sup>The non-thermal component of the electron energy spectrum is usually characterized as a power-law tail:  $dn_e/dE \propto E^{-\alpha}$ , where  $n_e$  and  $E$  are the electron density and energy, and  $\alpha$  is the so-called spectral index of the tail.

eration is the dissipation of large scale motions, typically provided by either the differential rotation of the disks, or by the expected MHD turbulence. Indeed, as the plasma is accreted, the presence of turbulence is needed to account for the (observationally supported) efficient outward transport of angular momentum in the disks. This turbulence is believed to be mainly provided by the so-called magnetorotational instability (MRI; [5]). Below we describe the three main mechanisms believed to contribute to this dissipation and subsequent particle heating. These are magnetic reconnection, turbulence damping, and viscous heating.

## Magnetic reconnection

Magnetic reconnection is a process that releases energy contained in magnetic field lines, producing a rapid heating of particles, which happens when magnetic field lines of opposite polarity come sufficiently close together (See Appendix F). In the context of collisionless plasmas, this process can occur in a non-thermal way, producing high-energy tails in the energy spectrum of the particles. Magnetic reconnection is currently being studied in the context of weakly collisional accretion disks around black holes, paying attention both to the energy partition between protons and electrons [46, 45], and to the possibility of electron and proton acceleration [6]. In [6] it was concluded that magnetic reconnection can be an efficient accelerator of particles, provided that the magnetization of the particles is very high. This magnetization is quantified through two different parameters:

- 1)  $\sigma \equiv B^2/4\pi\rho c^2$  (where  $B$  is the magnetic field intensity,  $\rho$  is the mass density of the plasma, and  $c$  the speed of light), and
- 2)  $\beta_j = 8\pi P_j/B^2$  (where  $P_j$  is the pressure of species “ $j$ ” ( $j$ =ions or electrons)).

Reconnection can produce hard non-thermal tails in the spectrum of electrons consistent with the observations described in the previous section [58, 6]. This acceleration, however, needs  $\sigma \gtrsim 1$  and  $\beta \lesssim 3 \times 10^{-3}$ . While  $\sigma \sim 1$  is a value that can occur in the disk corona, especially in the closest regions to the black hole, the condition  $\beta_e \lesssim 3 \times 10^{-3}$  appears to be rather restrictive. This can be seen from MHD simulations of weakly collisional accretion flows, for example, the figures 4 and 5 of [9] show that the typical values in the disk corona are  $\beta_e \sim 0.1 - 1$ .

## MHD turbulence damping

When non-linear MHD waves are present in the plasma, the interaction between different wave packets can transfer energy to shorter wavelength modes. This process is usually referred to as turbulence cascade, and can in principle reach wave-numbers  $k$  that satisfy  $kR_{L,i} \sim 1$  and  $kR_{L,e} \sim 1$ , where  $R_{L,j}$  is the Larmor radius of species  $j$ , as can be seen in [24] ( $R_{L,j} \equiv v_{th,j} \frac{m_j c}{q_j B}$ , where  $v_{th,j} \equiv (k_B T_j / m_j)^{1/2}$ ,  $m_j$  and  $q_j$  are the mass and charge of species  $j$ , and  $k_B$  is the Boltzmann constant). When  $k$  reaches these small scales, the waves can resonate with the particles gyro-orbit around the local magnetic field, allowing the transfer of energy from the waves to the particles (see §3.3).

Several studies using both analytic theory [41, 28] and MHD simulations (e.g., [33]) have proposed models for the heating of both electrons and protons due to turbulence damping in plasma conditions suitable to accretion disk environments. The main drawback, however, is their lack of consistency, in the sense that the back-reaction of the heated particles on the turbulence evolution is in most cases ignored<sup>3</sup>. Nevertheless, these types of studies do suggest the damping of MHD turbulence can be an important source of particle heating in systems like weakly collisional accretion disks, and that it can even produce significant non-thermal acceleration of relativistic electrons in these environments [34].

## Viscous heating

In the absence of collisions, if the background magnetic field grows sufficiently slowly, a pressure anisotropy with respect to the magnetic field direction will naturally develop in all species. This is a consequence of the conservation of the magnetic moment of particles (as we explain in Appendix A). This anisotropy satisfies  $P_{\perp,j} > P_{\parallel,j}$ , where  $P_{\perp,j}$  ( $P_{\parallel,j}$ ) is the pressure of species  $j$  perpendicular (parallel) to the direction of the field.

When the background magnetic field grows due to a velocity shear in the plasma, the presence of the anisotropy gives rise to the so-called “anisotropic viscosity”, which heats the plasma (as we explain in further details in Appendix D). When the pressure anisotropies of the different species surpass a certain limit, they can destabilize various electromagnetic plasma waves. These are the so-called “pressure anisotropy-driven instabilities”. The most relevant of these instabilities for this study are: the whistler instability [21], which is mainly driven by the electrons, and the ion-cyclotron (IC) and mirror instabilities [2, 27, 53], which are mainly driven by the ions. One important role of these instabilities is thus to regulate the viscous heating of the plasma. Therefore, understanding the behavior of the instabilities is essential to quantify the role of viscous heating in energizing the different species.

Furthermore, it has been recently shown that in the context of viscous heating the electrons can be accelerated stochastically to non-thermal regimes. This process happens via the second-order Fermi acceleration, which occurs due to the interaction between electrons and whistler waves [42]. Remarkably, this acceleration mechanism can produce a non-thermal tail that can be modeled as a power-law with spectral index  $\alpha \sim 3.7$ , which is close to the inferred index from the radio observations of Sgr A\* in its quiescent state as we mentioned above. This mechanism is in principle less restrictive than magnetic reconnection, in the sense that it works in the regime of  $\sigma \ll 1$  and for  $\beta_e \sim 0.1 - 1$ .

Given the importance of second-order Fermi acceleration of electrons in the cases of heating by anisotropic viscosity, in the next section we briefly describe this process.

---

<sup>3</sup>The only exception, to the best of our knowledge, is given by [62], who presents fully consistent PIC simulations of particle energization by MHD turbulence in the regime relevant for low collisionality accretion disk around black holes.

## Second-order Fermi Acceleration

The second-order Fermi acceleration of electrons occurs as they move along the background magnetic field  $\vec{B}$  and are scattered by whistler wave packets, which travel preferentially along  $\vec{B}$ . Because of the motion of the wave packets, one can show that the electron scattering is inelastic and that, on average, it produces a gain in the electron energy for a pitch angle variation of  $\sim \pi$  given by

$$\left\langle \frac{\Delta E}{E_{kin}} \right\rangle \approx \frac{8}{3} \gamma_o^2 \frac{U_o^2}{U_p^2} \left( \frac{\gamma_p + 1}{\gamma_p} \right) \quad (1)$$

(see Appendix E). In Equation 1,  $\frac{\Delta E}{E_{kin}}$  is the difference of the energies after and before the pitch angle change, normalized by the initial kinetic energy,  $U_o$  and  $\gamma_o$  are the speed and Lorentz factor of the wave packet, and  $U_p$  and  $\gamma_p$  are the speed and the Lorentz factor of the particle.

It is important to emphasize, however, that the results presented by [42] consider infinitely massive ions. The dynamics of the ions (in particular the IC and mirror instabilities) was neglected and, as a consequence, it had no possibility to affect the electrons dynamics. This raises the question of whether the ions can transfer part of their kinetic energy to the electrons via wave-particle interactions. Indeed, recently it has been suggested that the IC instability can transfer some of the energy of the ions to the electrons [50, 49] working as an “effective” ion-electron collisionality, even in absence of Coulomb collisions. The results of [50, 49] are however focused on the exponential phase of growth of the IC instability, and consider an initial temperature ratio  $T_{0e}/T_{0i} \lesssim 0.2$ .

Motivated by these findings, the goal of this thesis is thus to quantify to what extent this electron energization by IC modes occurs in the non-linear regime of the IC instability, i.e., after its exponential growth regime. In particular, we will pay special attention to the possibility of this energization giving rise to a non-thermal tail in the electron spectrum. We believe that capturing the non-linear regime of the IC instability is important because this regime should be dominant in the case of a plasma falling into a black hole. This is simply because the magnetic field is expected to be amplified during most of this process. The exponential growth of the IC modes should be considered, therefore, as a transient regime, that does not represent what happens most of the time.

Furthermore, we will concentrate on a regime not considered in [50, 49]. In our case we will consider moderate temperatures ratios (in particular we will test  $T_i/T_e = 1$  and 3). In this regime, the scattering of the ions may not be fully dominated by the IC instability. Indeed, the mirror modes would be dominant if  $\beta_i$  is sufficiently large. So we will focus on the cases when  $\beta_i \lesssim 1$ , in which the IC instability should dominate. Since the two electromagnetic modes expected to be dominant for  $\beta_i \lesssim 1$ , the IC and whistler instabilities, have their wave-vector quasi-parallel to the mean magnetic field, many of our simulations will be one-dimensional (1D). In these simulations only modes that propagate parallel to  $\vec{B}$  are captured. The scheme to implement our 1D simulations is explained in Appendix H.

# Chapter 1

## The physical situation and simulation setup

As we say above, our goal is to study the electron energization by IC modes in a collisionless plasma. This transfer of energy has indeed been found to occur, but only in the exponential growth regime of the IC instability and when  $T_e/T_i \lesssim 0.2$  [50, 49]. The goal of this thesis is thus to investigate the regime  $T_e/T_i \gtrsim 0.2$ , and focusing on the non-linear, saturated stage of the IC instability. In this chapter we describe the physical situation under which we believe that this energization can occur.

### 1.1 The physical situation

The physical situation that we want to study corresponds to a homogeneous plasma subject to a shear motion. This situation is expected to be ubiquitous in accretion disks, where local shear motions should exist either due to the differential rotation of the disk, or due to the MHD turbulence expected in these disks, which is most likely produced by the magnetorotational instability (MRI; [5]).

In this shearing setup, several physical processes should occur simultaneously:

1. The magnetic field is amplified due to magnetic flux conservation (see Appendix C)
2. A pressure anisotropy with respect to the local magnetic field arises, due to the conservation of the magnetic moment of the particles (see Appendix A).
3. The pressure anisotropy in presence of a shearing plasma motion gives rise to heating by the so-called “anisotropic viscosity”. This heating rate is given by

$$\frac{du_e}{dt} = q\Delta P_e \quad (1.1)$$

where  $u_e$  is the internal energy of the electrons,  $q$  is the growth rate of the magnetic field and  $\Delta P_e = P_{\perp,e} - P_{\parallel,e}$  (see Appendix D).

4. If the pressure anisotropy is large enough, kinetic plasma instabilities like the mirror, IC and whistler instabilities are triggered, providing efficient pitch-angle scattering to the particles.

An important aspect of this setup is that it captures the non-linear, saturated state of the instabilities. This is because it allows the magnetic field to grow for a time significantly larger than the initial exponential growth regime of the instabilities. We believe that this setup is astrophysically realistic, since in accretion disks the magnetic field is most likely amplified most of the time. In what follows we describe our simulation setup, which is intended to capture all these processes self-consistently.

## 1.2 Simulation setup

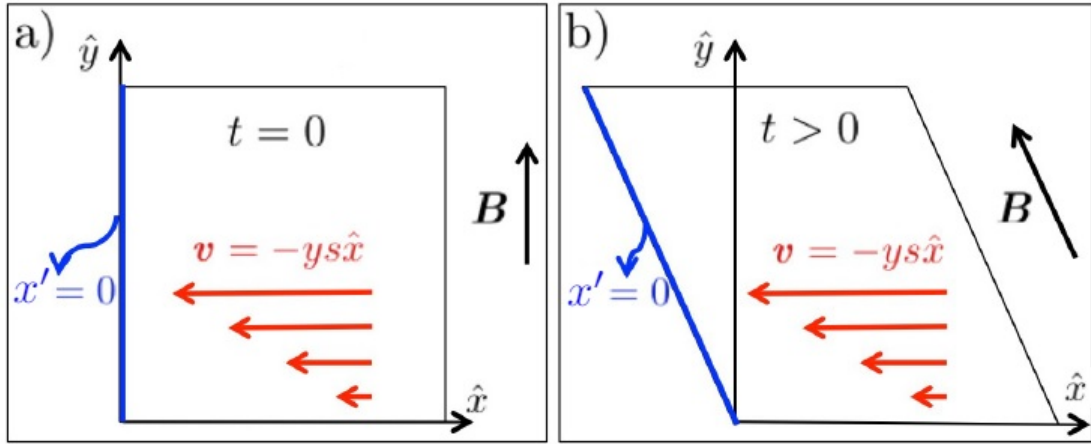


Figure 1.1: Panels a and b show a sketch of the simulation domain in our 2D simulations at  $t = 0$  and  $t > 0$ , respectively. The 2D domain follows the shearing flow of the plasma (red arrows), acquiring a parallelogram shape. Magnetic flux conservation changes the magnitude and orientation of the background magnetic field  $\mathbf{B}$ , which is always parallel to the diagonal sides of the parallelogram. The blue lines show the domain of our 1D runs.

In this thesis we simulate plasmas from first principles using the “particle-in-cell” (PIC) simulation method, making use of the PIC code TRISTAN-MP [8] (In Appendix G we describe the PIC method). We set up a shearing plasma made of ions and electrons. In this case the plasma is initially in presence of a homogeneous initial magnetic field that points along the  $y$  axis,  $\mathbf{B} = B_0 \hat{y}$ . This field is amplified by imposing a shear plasma velocity  $\mathbf{v} = -sy\hat{x}$  (represented by red arrows in Figure 1.1a), where  $y$  is the distance along  $\hat{y}$  and  $s$  is the shear rate (assumed constant). This way, the background magnetic field  $\mathbf{B}$  in the simulation increases continuously and changes direction due to magnetic flux conservation, with its  $x$ -component evolving as  $dB_x/dt = -sB_0$ , while  $dB_y/dt = dB_z/dt = 0$  (Figure 1.1b shows how  $\vec{B}$  changes orientation for  $t > 0$ ). Due to the conservation of  $\mu_j (\equiv \frac{P_{\perp,j}}{2B})$ , where  $P_{\perp,j}$  is the pressure perpendicular to the magnetic field of species  $j$ ), this magnetic growth drives  $P_{\perp,j} > P_{\parallel,j}$  during the whole simulation allowing the triggering of kinetic instabilities that limit the pressure

anisotropies (see Appendix A for an explanation of why  $\mu_j$  should be conserved).

Our 2D runs use initially square simulation domains (as the one depicted in Figure 1.1a) that follow the mean shear motion of the plasma. This makes the 2D domain acquire a parallelogram shape for  $t > 0$  (as shown in Figure 1.1b). This continuous modification of the simulation domain is handled through the use of the so-called ‘shearing coordinates’, which are described in the Appendix of [43]. In our 1D runs, on the other hand, the simulation domain corresponds to the blue line shown in Figures 1.1a and 1.1b, which also moves with the shearing flow. Since the symmetry axis of this 1D domain is permanently parallel to  $\mathbf{B}$ , our 1D approach allows to capture waves that propagate parallel to  $\mathbf{B}$ . The self-consistent implementation of the 1D runs requires a change in the definition of our shear coordinates, which is explained in detail in Appendix H.

Our plasma parameters are the initial temperature of electrons and ions ( $T_e$  and  $T_i$ ). Throughout this thesis we choose these temperatures to be  $k_B T_e = k_B T_i = 0.1 m_e c^2$ , which is a value representative of the inner region of accretion disks around black holes. The other plasma parameters are the initial ratio between electron pressure and magnetic pressure ( $\beta_e^{init}$ ), the ion to electron mass ratio  $m_i/m_e$ , and the electron ‘magnetization’, which quantifies the ratio between the initial electron cyclotron frequency ( $\omega_{c,e}^{init}$ ) and  $s$  ( $\omega_{c,e}^{init} = q_e B_0 / m_e c$ , with  $q_e$  and  $B_0$  being the magnitude of the electron and ion electric charges and the initial magnetic field, respectively).

It is important to emphasize that  $m_i/m_e$  and  $\omega_{c,e}^{init}/s$  have in reality relatively well defined values and, therefore, they should not be considered as free parameters in the study. However, using realistic values for these quantities is out of reach for our current computational capabilities. Therefore our approach will be to consider  $m_i/m_e$  and  $\omega_{c,e}^{init}/s$  as free parameters, and use the simulation to understand the role that they may play in the transfer of energy from ions to electrons.

The numerical parameters in our runs are: the number of macro-particles per cell ( $N_{ppc}$ ), the electron skin depth in term of grid point spacing ( $c/(\omega_{p,e}\Delta x)$ , where  $\omega_{p,e} = 4\pi n_e q_e^2/m_e$  is the electron plasma frequency and  $n_e$  is the electron density), and the box size in terms of the initial electron Larmor radius ( $L/R_{L,e}^{init}$ ). Table 1.1 shows a summary of our key simulations. We ran a series of simulations ensuring that the numerical parameters do not affect our result. The runs used just for numerical convergence are not in Table 1.1.

| Run | $T_i/T_e$ | $\omega_{ce}^{init}/s$ | $m_i/m_e$ | $\beta_e^{init}$ | $N_{ppc}$ | $c/(\omega_{pe}^{init}\Delta x)$ | $L/R_{Le}^{init}$ | Dimension |
|-----|-----------|------------------------|-----------|------------------|-----------|----------------------------------|-------------------|-----------|
| FC1 | 1         | 1600                   | 2         | 0.5              | 160       | 18                               | 85                | 2D        |
| FC2 | 1         | 1600                   | 2         | 0.5              | 640       | 48                               | 104               | 1D        |
| FC3 | 1         | 1600                   | 2         | 2                | 160       | 8                                | 120               | 2D        |
| FC4 | 1         | 1600                   | 2         | 2                | 320       | 36                               | 83                | 1D        |
| OE1 | -         | 1500                   | $\infty$  | 2                | 480       | 15                               | 40                | 1D        |
| OE2 | -         | 3000                   | $\infty$  | 2                | 480       | 10                               | 52                | 1D        |
| MR1 | 1         | 1500                   | 4         | 2                | 720       | 10                               | 84                | 1D        |
| MR2 | 1         | 1500                   | 12        | 2                | 500       | 15                               | 139               | 1D        |
| MR3 | 1         | 1500                   | 16        | 2                | 700       | 15                               | 160               | 1D        |
| MR4 | 1         | 3000                   | 4         | 2                | 720       | 10                               | 84                | 1D        |
| MR5 | 1         | 3000                   | 12        | 2                | 960       | 10                               | 148               | 1D        |
| MR6 | 1         | 3000                   | 16        | 2                | 960       | 10                               | 172               | 1D        |
| TR1 | 3         | 1500                   | 4         | 2                | 720       | 8                                | 150               | 1D        |
| TR2 | 3         | 1500                   | 12        | 2                | 1440      | 8                                | 255               | 1D        |
| TR3 | 3         | 1500                   | 16        | 2                | 1440      | 8                                | 300               | 1D        |
| TR4 | 3         | 3000                   | 4         | 2                | 1440      | 8                                | 150               | 1D        |
| TR5 | 3         | 3000                   | 12        | 2                | 1440      | 8                                | 150               | 1D        |
| TR6 | 3         | 3000                   | 16        | 2                | 1440      | 8                                | 300               | 1D        |

Table 1.1: Set of simulations performed in this thesis, with their physical and numerical initial conditions, which are the initial temperature ratio between species ( $T_i/T_e$ ), the magnetization of the electrons quantified as the initial cyclotron frequency over the shear rate ( $\omega_{ce}^{init}/s$ ), the mass ratio between species ( $m_i/m_e$ ), the initial beta parameter of the electrons ( $\beta_e^{init}$ ), which is the electron pressure over the magnetic pressure, the number of macro-particles per cell in the simulation ( $N_{ppc}$ ), the plasma skin depth over the grid length ( $c/(\omega_{pe}\Delta x)$ ), and the spatial length of the simulation in terms of the electrons initial Larmor radius ( $L/R_{Le}^{init}$ , where  $R_{Le}^{init} = v_{th}^{init}/\omega_{ce}^{init}$ ). Also, we performed convergence tests for the numerical parameters,  $N_{ppc}$ ,  $L/R_{Le}^{init}$ , and  $c/(\omega_{pe}\Delta x)$ .

# Chapter 2

## Suitability of the 1D approach

As stated above, the goal of this thesis is to study the possibility of electron energization by IC modes. Since the evolutions of ions and electrons involves very different time and length scales, capturing simultaneously the ion and electron dynamics is computationally challenging. In order to alleviate this problem, in this thesis we will make use of 1D simulations, which use the fact that the dominant wave vectors in the regime of interest to us (where the ion scattering is dominated by the IC modes, instead of the mirror modes) are nearly parallel to the background magnetic field.

Thus in §2.1 we will show that the 1D approach provides results quite similar to 2D simulations in the regime where the ion scattering is mainly provided by the IC instability. When the ion scattering is dominated by the mirror instability, the 1D approach is not enough to correctly capture the wave-particle interaction for ions and electrons, and 2D simulations are needed. This idea is reinforced in §2.2, where we use Fourier analysis to show that 1D simulations are capable to capture correctly the main characteristics of the IC and whistler modes (which are driven mainly by the ion and electron pressure anisotropies, respectively).

### 2.1 Comparing 1D and 2D simulations

Figure 2.1 shows the fluctuations in the three magnetic field components  $\delta B_i \equiv (B_i - \langle B_i \rangle) / B_0$  (where  $i=x,y,z$  and  $\langle \cdot \rangle$  is the spatial mean), at  $t \cdot s = 2$ , for the 2D simulations FC1 (upper row), and FC3 (lower row). These simulations use the same ion and electron temperatures (with  $k_B T_e / m_e c^2 = 0.1$ ), the same ion to electron mass ratio  $m_i / m_e = 2$ , and the same ion magnetization  $\omega_{c,i}^{\text{init}} / \Omega_i = 800$ . The difference between these runs is only in the intensity of their magnetic fields, which imply that the FC1 and FC3 runs have  $\beta_e^{\text{init}} = 0.5$  and  $\beta_e^{\text{init}} = 2$  ( $\beta_e^{\text{init}} = \beta_i^{\text{init}}$ ), respectively. The arrows show the magnetic field direction on the  $x - y$  simulation plane.

Figures 2.1b and 2.1c show that the dominant modes in the simulation with  $\beta_e^{\text{init}} = 0.5$  propagates almost parallel to the mean magnetic field  $\langle \mathbf{B} \rangle$ . This is a characteristic of the IC

modes [19], whose maximum growth rate occurs at  $\vec{k} \times \langle \mathbf{B} \rangle = 0$ . Figure 2.1a, on the other hand, shows modes with wave vector parallel to  $\langle \mathbf{B} \rangle$  and subdominant oblique modes [18]. Since the mirror modes are characterized by being mainly oblique, this indicates that the mirror modes are present at a subdominant level when  $\beta_i^{init} = 0.5$ . For the simulation with  $\beta_e^{init} = 2$ , Figure 2.1d shows the dominance of oblique mirror modes, while Figure 2.1e shows that the IC modes are strongly suppressed. The IC modes are, however, still clearly seen in  $\delta B_z$  (Figure 2.1f). This is because in the regime of low  $\beta_i$  and low anisotropy the magnetic fluctuations associated to the mirror instability are in the plane which contains  $\vec{k}$  and  $\mathbf{B}$  [22].

The different modes triggered by the pressure anisotropy grow exponentially after the anisotropy reaches a threshold value. Indeed, the expectation is that the growth of the anisotropy initially follows the prescription given by the adiabatic (CGL; [13]) equation of state (see Appendix A), which in this case implies a growth of  $P_{\perp,j}$  and a decrease of  $P_{\parallel,j}$ . When the threshold is reached, the fluctuations in the magnetic field scatter particles, driving the plasma to a more isotropic state and breaking the CGL evolution. The growth of the anisotropy heats the plasma due to the anisotropic viscosity [30], as we show in Appendix D. This heating mechanism is due to the so-called ‘‘anisotropic viscosity’’, and occurs regardless of the interaction between species, and independently of the interaction that each species could have with the electromagnetic fields.

Figure 2.2 shows that the main results of the 2D simulations are well reproduced in our 1D runs. The top row shows the energy contained in the magnetic field fluctuations, for runs that simulate exactly the same physical situations, but in 1D (dashed lines) and 2D (solid lines). In order to help distinguishing the contributions of the whistler, IC and mirror instabilities,  $\delta \mathbf{B}$  is separated into fluctuations parallel (blue lines), and perpendicular (red lines) to the mean magnetic field.

Panel 2.2a shows simulations with  $\beta_e^{init} = 0.5$  (runs FC1 and FC2 in Table 1.1). We see that the fluctuations perpendicular to the mean magnetic field are dominant in the 2D runs until  $t \cdot s \sim 2.3$ . Since these fluctuations are expected to be mainly produced by the whistler and IC instabilities, we conclude that the  $\beta_e^{init} = 0.5$  regime is dominated by these modes. Remarkably, the evolution of these perpendicular fluctuations is fairly well reproduced in the 1D simulations, which indicates the suitability of the 1D approach in the regime where IC and whistler modes dominate. The parallel fluctuations, which are not allowed in 1D simulations, gain sufficient energy in 2D to be dominant at the end of the simulations ( $t \cdot s \gtrsim 2.3$ ), so the simulation 1D can reproduce correctly the excitation of pressure anisotropy-driven instabilities until  $t \cdot s \sim 2.3$ . For the 2D simulations with  $\beta_e^{init} = 2$  (panel 2.2b) the fluctuations parallel to the mean magnetic field are the most energetic modes from near the begin of the simulation. These fluctuations are related to the mirror modes, which are not captured with simulations in 1D. However, the perpendicular fluctuations are relatively close to what is obtained in the 1D simulations ( $\sim 3$  times smaller), and evolve similar to the case  $\beta_e^{init} = 0.5$  with the difference that the exponential growth of the fluctuations begins a little earlier ( $t \cdot s \sim 0.7$ ).

Figures 2.2c and 2.2d shows the energy gain of electrons for the same simulations shown in Figure 2.2a and 2.2b, respectively. These figures show the actual electron energy gain (green line), and the expected heating by anisotropic viscosity (blue line), which considers

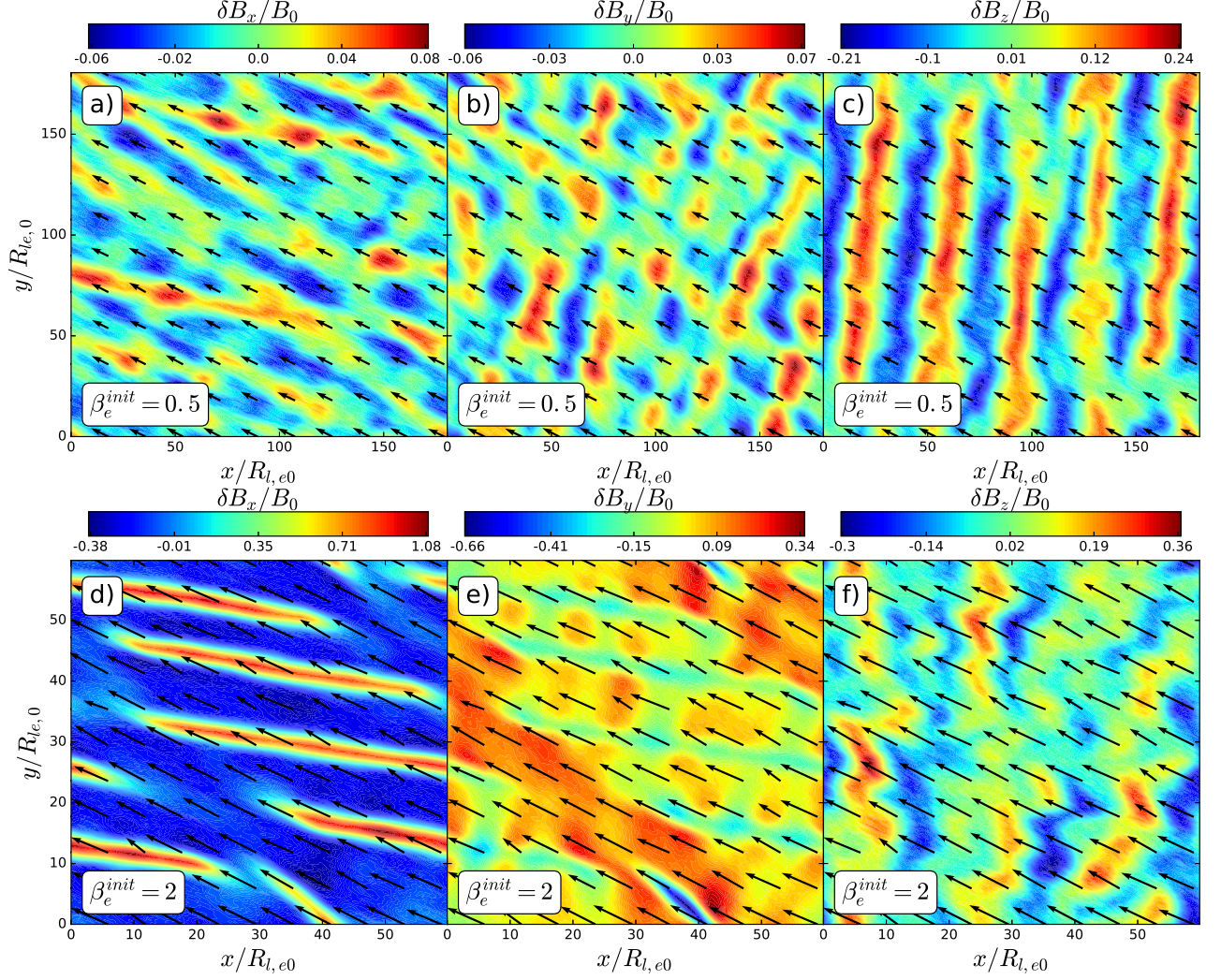


Figure 2.1: Fluctuations in the magnetic field separated by components at time  $t \cdot s = 2$ . The upper row corresponds to simulation FC1 ( $m_i/m_e = 2$  and  $\beta_e^{init} = 0.5$ ), and the lower row corresponds to simulation FC3 ( $m_i/m_e = 2$  and  $\beta_e^{init} = 2$ ). The fluctuations are normalized by the initial magnetic field in the simulations  $B_0$ , and the black arrows show the magnetic field direction on the  $x - y$  simulation plane. The IC modes, with wave vector  $\vec{k}$  quasi-parallel to the mean magnetic field  $\langle \mathbf{B} \rangle$ , are dominant in the case with  $\beta_e^{init} = 0.5$ . And the mirror modes, with wave vector oblique to the mean magnetic field, are dominant in the case  $\beta_e^{init} = 2$ .

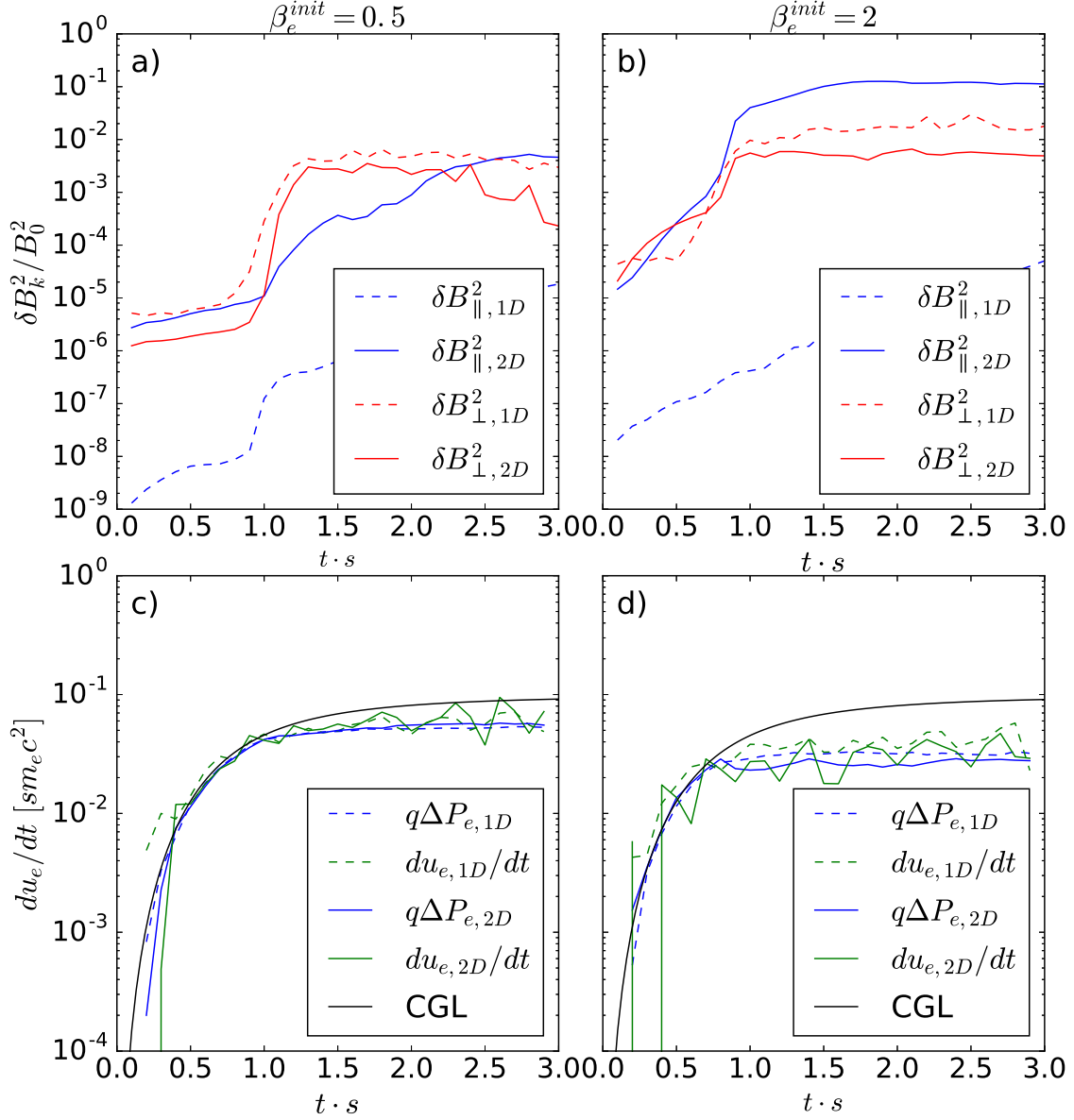


Figure 2.2: Comparison between simulations in one and two dimensions. The solid lines represents the values in two-dimensional simulations (FC1 and FC3), while the dashed lines show the same quantities for one-dimensional simulations (FC2 and FC4). The left and right column correspond to the simulations with  $\beta_e^{init} = 0.5$  and  $\beta_e^{init} = 2$ . The upper row shows the energy contained in the parallel (blue lines) and perpendicular (red lines) fluctuations of the magnetic field normalized by the initial magnetic field energy. The bottom row shows the heating rate (green lines), the prediction by viscous heating considering the anisotropy in the simulation (blue lines), and the viscous heating considering the CGL prediction for the anisotropy and the evolution of the magnetic field (black line). These quantities are normalized by the electron rest mass energy multiplied by  $s$ .

the electron anisotropy obtained from the simulations. The 1D and 2D cases are shown in dashed and solid lines, respectively. Electron heating is well described by the anisotropic viscosity (with an error of  $\sim 10\%$ ) both in 1D and 2D. But most importantly, 1D and 2D results are almost indistinguishable between each other. This implies that the electron anisotropy thresholds in both simulations are essentially the same. Figure 2.2d shows the same quantities but in the case  $\beta_e^{init} = 2$ . In this case the correspondence between electron heating and anisotropic viscosity occurs to the same level as in the case  $\beta_e^{init} = 0.5$ , both in 1D and 2D. However, in the 1D simulation the electrons are heated more than the two-dimensional simulation. Consistently the anisotropy and the viscous heating obtained in 1D is greater than in 2D. This is consistent with 2D runs having more possible unstable modes, given that they are not limited to only parallel modes. In this particular case, the mirror modes get unstable before the IC modes. Thus, since the mirror modes are expected to reduce somewhat the electron anisotropy (e.g. [44]), the electron anisotropy grows to a lower level compared to what happens in the 1D runs.

In order to see when the electron anisotropy stops evolving according to the CGL equation of state, in Figures 2.2c and 2.2d we show the viscous heating assuming the CGL prescription (solid black). We see that the CGL equation of state stops being valid at  $t \cdot s \sim 1$  and  $\sim 0.7$ , respectively. These times coincide fairly well with the moments where the instabilities grow exponentially, as can be seen from Figures 2.2a and 2.2b. This is consistent with the CGL regime being broken by the efficient pitch-angle scattering provided by the instabilities.

In summary, Figure 2.2 shows that the 1D simulations describe quite well the evolution of electron energy gain in a regime where the ion pitch-angle is dominated by the IC instability. In this regime, the expected modes in the 1D simulations are the ion-cyclotron and whistler which are triggered by the anisotropy of the ions and electrons respectively. This implies that we can use 1D simulations to study the potential transfer of energy from ions to electrons through their interaction with IC waves, which is the focus of this thesis. In the next section we use Fourier analysis to provide further evidence that our 1D simulations are indeed dominated by IC and whistler modes. In order to identify the presence of the IC and whistler modes, we will use the fact that these modes have left-handed and right-handed circular polarizations, respectively.

## 2.2 Fourier Analysis

In our simulations the mean magnetic field is in the  $x-y$  plane, and the whistler and IC modes have fluctuations perpendicular to the mean magnetic field. This implies that the magnetic field in the  $\hat{z}$  axis is perpendicular to  $\langle \vec{B} \rangle$  ( $\delta B_z$ ), and the other perpendicular component is contained in the  $x-y$  plane (which we call  $\delta B_{\perp,xy}$ ). In order to find the presence of the IC and whistler modes we combine the Fourier transforms of both perpendicular components of  $\delta \vec{B}$  as:

$$\delta \tilde{B}_{\perp} = \delta \tilde{B}_z - i \delta \tilde{B}_{\perp,xy}, \quad (2.1)$$

where the tilde indicates the Fourier transform of a quantity. Using the combination  $\delta\tilde{B}_\perp$  the modes with right-handed circular polarization appear with positives frequencies ( $\omega > 0$ ), while the modes with left-handed circular polarization appear with negative frequency ( $\omega < 0$ ). In order to show this property of  $\delta\tilde{B}_\perp$  we applied it to runs OE1 and MR3. The simulation OE1 only considers the dynamics of the electrons, with the ions only neutralizing the charge and not contributing to the current. In this setup, thus, only whistler modes should grow. For the simulation MR3, we consider electrons under the same conditions as in run OE1, but with ions with finite mass  $m_i = 16m_e$ , resulting in the growth of both IC and whistler modes.

Thus, when calculating  $\delta\tilde{B}_\perp$  for the run OE1 and for times between  $0.7 \leq t \cdot s \leq 0.8$  and  $2.4 \leq t \cdot s \leq 2.5$  we get the results shown in Figure 2.3a and 2.3c. The power obtained corresponds to the whistler modes, as it is verified by comparing with the theoretical dispersion relation for long-wavelength modes. This theoretical calculation considers the non-relativistic bi-Maxwellian distribution function, and it was done using standard kinetic plasma theory in a hot magnetized plasma [26]. One important limitation of this comparison with theory is that (as we will see below) the particle spectra obtained in our simulations are typically not completely well described by bi-Maxwellian distributions. Despite this, the dispersion relations obtained from the theory and from the simulations agree fairly well in the long wavelength limit.

In case of run MR3, we separate both modes in the same way as in simulation OE1 and for the same times. In Figure 2.3b we can see the dispersion relation between  $0.7 \leq t \cdot s \leq 0.8$ . Curiously only the whistler modes are present in this range of time. Indeed, for this time interval both simulations have similar dispersion relation. In the panel 2.3d we show  $\delta\tilde{B}_\perp$  for run MR3 and for  $2.4 \leq t \cdot s \leq 2.5$ . In this range of time both modes are present, with the IC modes represented by negatives frequencies. Here we also compare with the analytical dispersion relation (black dashed line) in the long-wavelength limit considering same anisotropy reached by the ions in the simulations. The whistler modes have a dispersion relation slightly different to the case of the infinitely massive ions, mainly in the low frequencies, where the modes in the fixed ions case have a shorter wavelength (higher  $k$ ) than the case with evolving ions.

The fact that the IC modes are not present in the early stage of run MR3 is also suggested by the evolution of the energy of the magnetic fluctuations. This is shown in Fig 2.4 for runs OE1 (dashed lines) and MR3 (solid lines). While for  $\delta B_\perp^2$  (red lines) we can see a single exponential growth regime in run OE1, for MR3 we can see two exponential growth regimes. These two growths (with the first one simultaneous with the exponential growth regime of run OE1) occur at  $t \cdot s \sim 0.5 - 0.7$  and  $t \cdot s \sim 1.1 - 1.3$ , and are consistent with the growth of the whistler and IC instabilities, respectively.

In summary, our 1D simulations describe consistently the evolution and propagation of the main instabilities expected in a plasma regime, dominated by modes parallel to the mean magnetic field. The presence of this modes allows the wave-particle interaction, which in principle, could be responsible for an energy transfer between species in an otherwise collisionless plasma. We will thus explore this possibility in the following sections making use of the computationally cheaper 1D simulations.

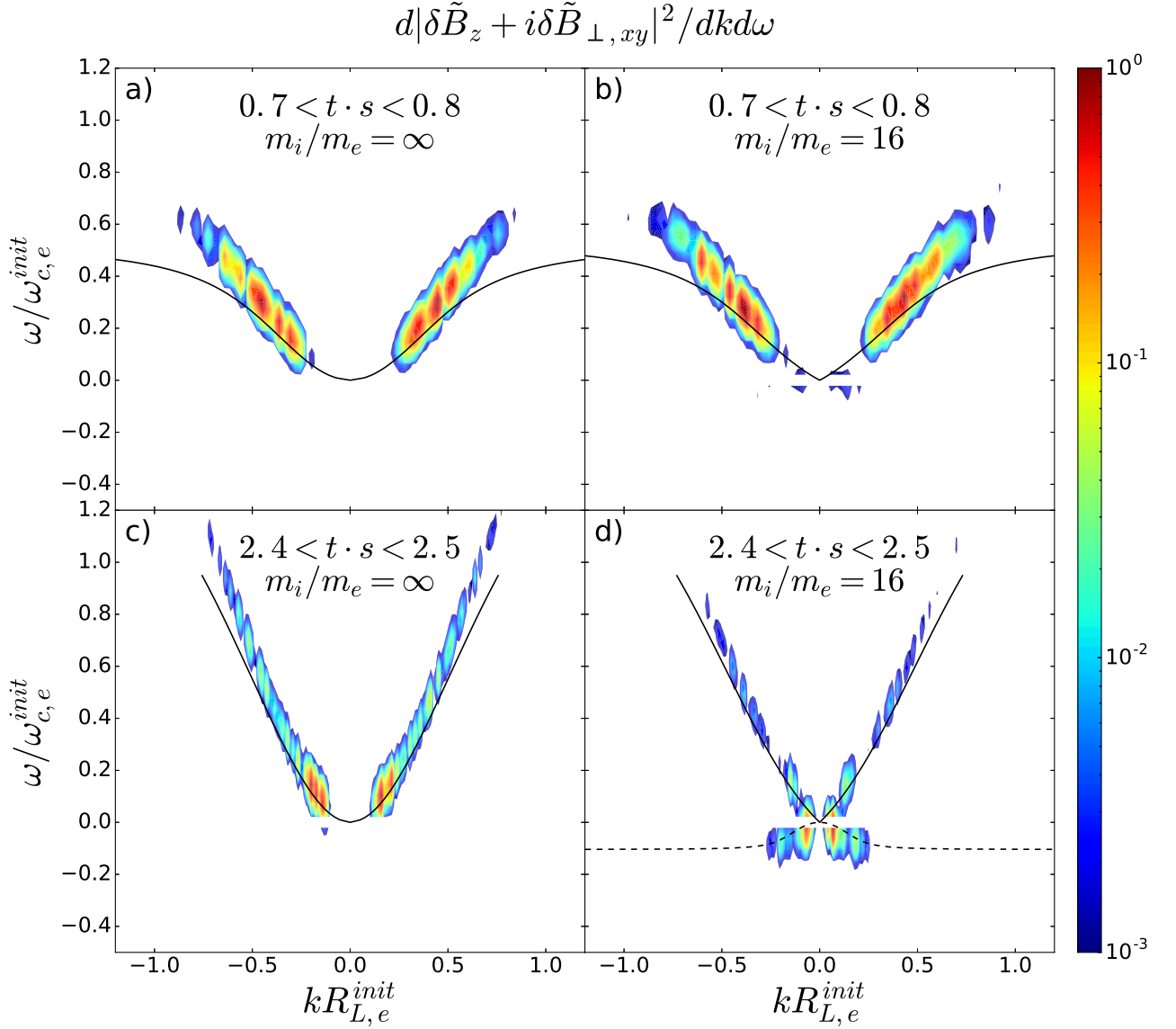


Figure 2.3: Dispersion relations for simulations OE1 (left column) and MR3 (right column) in different ranges of time:  $0.7 \leq t \cdot s \leq 0.8$  (top row) and  $2.4 \leq t \cdot s \leq 2.5$  (bottom row). The color bars show the energy density per range of  $k$  and  $\omega$  normalized by its maximum value. The black lines show the theoretical dispersion relation in the long wavelength limit considering a bi-Maxwellian distribution with the same anisotropy reached in the simulations. The solid black lines show the dispersion relation for whistler modes, and the black dashed line shows the IC mode.

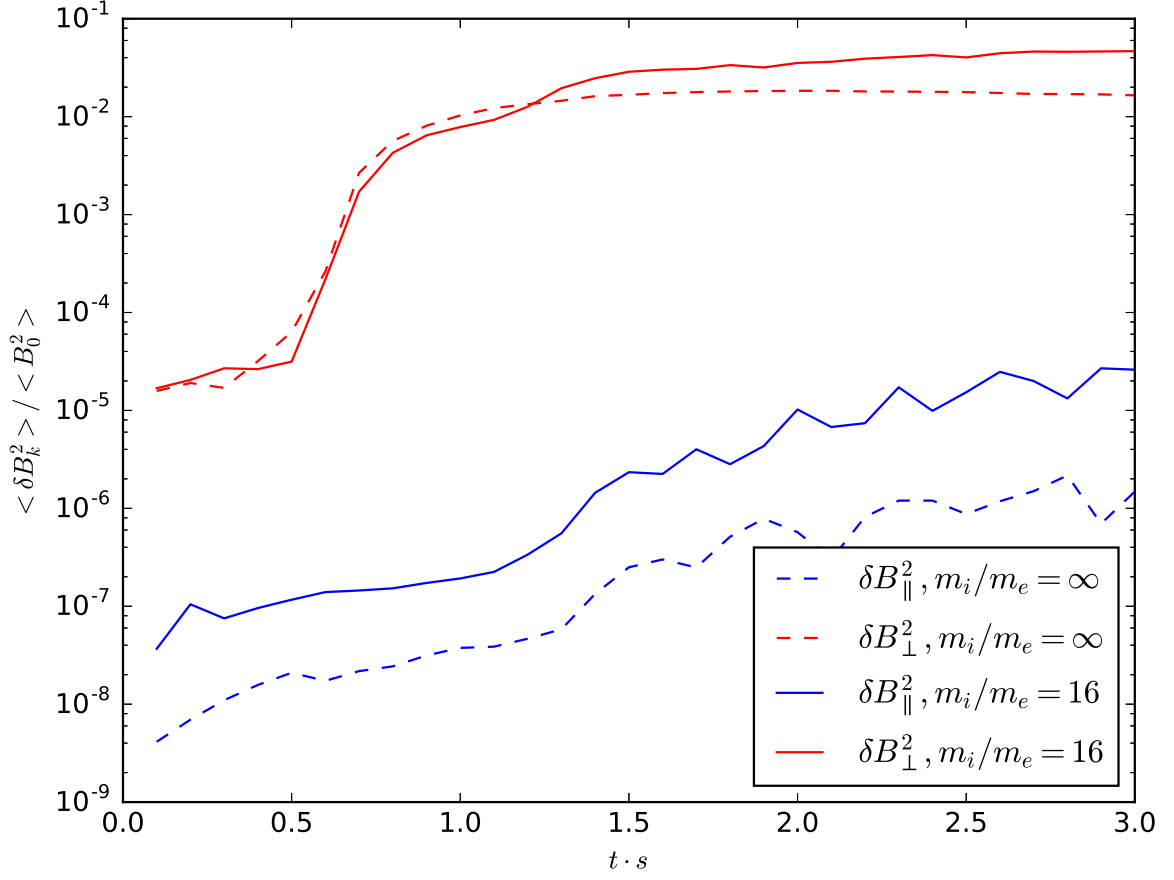


Figure 2.4: Evolution of the energy contained in the fluctuations of the magnetic field for simulation OE1 ( $m_i/m_e = \infty$  and  $\omega_{c,e}^{init} = 1500$ ) in dashed lines and MR3 ( $m_i/m_e = 16$  and  $\omega_{c,e}^{init} = 1500$ ) in solid lines. The fluctuations are separated into components parallel (blue lines), and perpendicular (red lines) to the direction of mean magnetic field, and are normalized by the energy of the initial magnetic field.

# Chapter 3

## Results

In the previous chapter we showed the suitability of 1D simulations for studying electron energization when the intervening instabilities involve mainly parallelly propagating modes. This implies that 1D simulations constitute a convenient tool to tackle the problem electron energization by IC modes.

In this thesis we study two main aspects of this problem. First, the overall electron heating, with focus on the case where the electrons are colder than the ions, which is expected in low luminosity accretion flows like in Sgr A\*. Second, the possible non-thermal acceleration of electrons. As we mentioned above, the waves that control the pressure anisotropy of particles via pitch-angle scattering can also produce stochastic acceleration. This was demonstrated for the case of electrons by [42], using simulations where only the electron dynamics was captured. In that case, the electron acceleration is produced by the propagating whistler waves. In this thesis we thus intend to explore the possibility for a similar effect to occur due to interaction between electrons and IC waves.

### 3.1 Electron Heating Rate

Rather than considering many plasma conditions, our study will focus on a reduced range of plasma parameters, hoping to understand the underlying physics involved in the potential ion to electron energy transfer. Thus, throughout this study we will concentrate on a case with  $\beta_e^{init} = 2$  and  $k_B T_e / m_e c^2 = 0.1$ . Although we showed above that in this regime the ion pitch-angle scattering is dominated by the mirror instability, we also saw that the IC modes are still present, with an amplitude very similar to the one obtained in our 1D simulations. Thus, the first 1D exploration should shed light on the role of ions in the electron energization. As we attain a better understanding of this interaction, our intention is indeed to extend our analysis to other values of  $\beta_e$ . Also, this mildly relativistic electron regime is likely relevant in the inner region of low luminosity accretion flows around black holes like Sgr A\*.

Since we want to estimate the possible electron heating due to IC modes, we will use control simulations with “inert ions”. This means that ions will be assumed to have infinite mass

and, therefore, they will not move.<sup>1</sup> We will thus compare these runs with the simulations where ions do have the ability to move, which will allow us to quantify the role played by the ions. For these simulations we will consider cases where ions and electrons have the same temperature ( $T_i/T_e = 1$ ) and also cases where  $T_i/T_e = 3$ , with the latter likely being relevant in “two temperature” systems like Sgr A\* and other low luminosity accretion flows.

Another important parameter in our simulations will be the mass ratio between ions and electrons. Using a realistic mass ratio ( $m_i/m_e = 1836$ ) is beyond our computational capabilities, even for the 1D runs. Because of this reason, in this study we are considering  $m_i/m_e$  as another free parameter, with the goal of determining the trend of the electron heating as this parameter grows. The goal underlying this approach is to reach an understanding of the role played by  $m_i/m_e$  that will allow us to make predictions on what would happen if  $m_i/m_e = 1836$ .

The last simulation parameter will be the ratio between the initial electron cyclotron frequency ( $\omega_{c,e}^{init}$ ) and  $s$ , which we have named “electron magnetization”. Using realistic values of  $\omega_{c,e}^{init}/s$  is also beyond the reach of our simulations resources. Indeed, in realistic astrophysical scenarios,  $\omega_{c,e}^{init}/s$  can reach values as high as  $10^{11} - 10^{12}$  (see, [40]). Thus, our approach will be also to understand the role played by  $\omega_{c,e}^{init}/s$  as a tool to quantify the degree to which ions can transfer their energy to electrons via the IC instability under realistic astrophysical conditions.

Figures 3.1a and 3.1b show in solid lines the electron heating rate in control runs OE1 and OE2, which use  $\omega_{c,e}^{init}/s = 1500$  and  $3000$ , respectively. For comparison, the dashed-black lines show the predicted heating by only anisotropic viscosity. At the beginning of the simulations, the electrons are heated mainly via spurious noise. After this first stage, the waves start to grow taking energy from the particles [38], which makes the heating rate of the electrons smaller than the viscous prediction, as it can be seen for  $0.5 \lesssim t \cdot s \lesssim 1$  in the two runs. This growth of the waves is indeed seen from Figures 3.1c and 3.1d, which show the energy in the fluctuations of the magnetic field (fluctuations components perpendicular and parallel to  $\langle \mathbf{B} \rangle$  in purple and green, respectively). These fluctuations grow when the electrons reach the necessary anisotropy to make the whistler modes grow on time scales sufficiently smaller than the evolution time of the system (which is given by  $\sim s^{-1}$ ). When this anisotropy is reached, the amplitude of the whistler modes grows exponentially until reaching a quasi-steady equilibrium. After reaching this regime, the electrons heating is well described by the viscous heating. In a realistic scenario the small decrease in the electron heating associated to the growth of the whistler waves is not significant, since it is only an initial transient in the formation of the modes. After this initial regime, the particles are mainly heated by the viscosity as it is shown for  $t \cdot s \gtrsim 1$  in figures 3.1a and 3.1b.

On the other hand, in simulations with finite mass ratio between ions and electrons, the electrons heating rate is slightly modified as seen in Figures 3.2a and 3.2b. These two figures correspond to runs MR1 and MR4, where the electrons are under exactly the same conditions as in runs OE1 and OE2, respectively, but in these cases the ions are mobile. This is achieved by giving the ions a mass 4 times larger than the one of the electrons ( $m_i/m_e = 4$ ), and using

---

<sup>1</sup>Of course, in these control simulations the ions still possess electric charge so that the plasma is globally neutral.

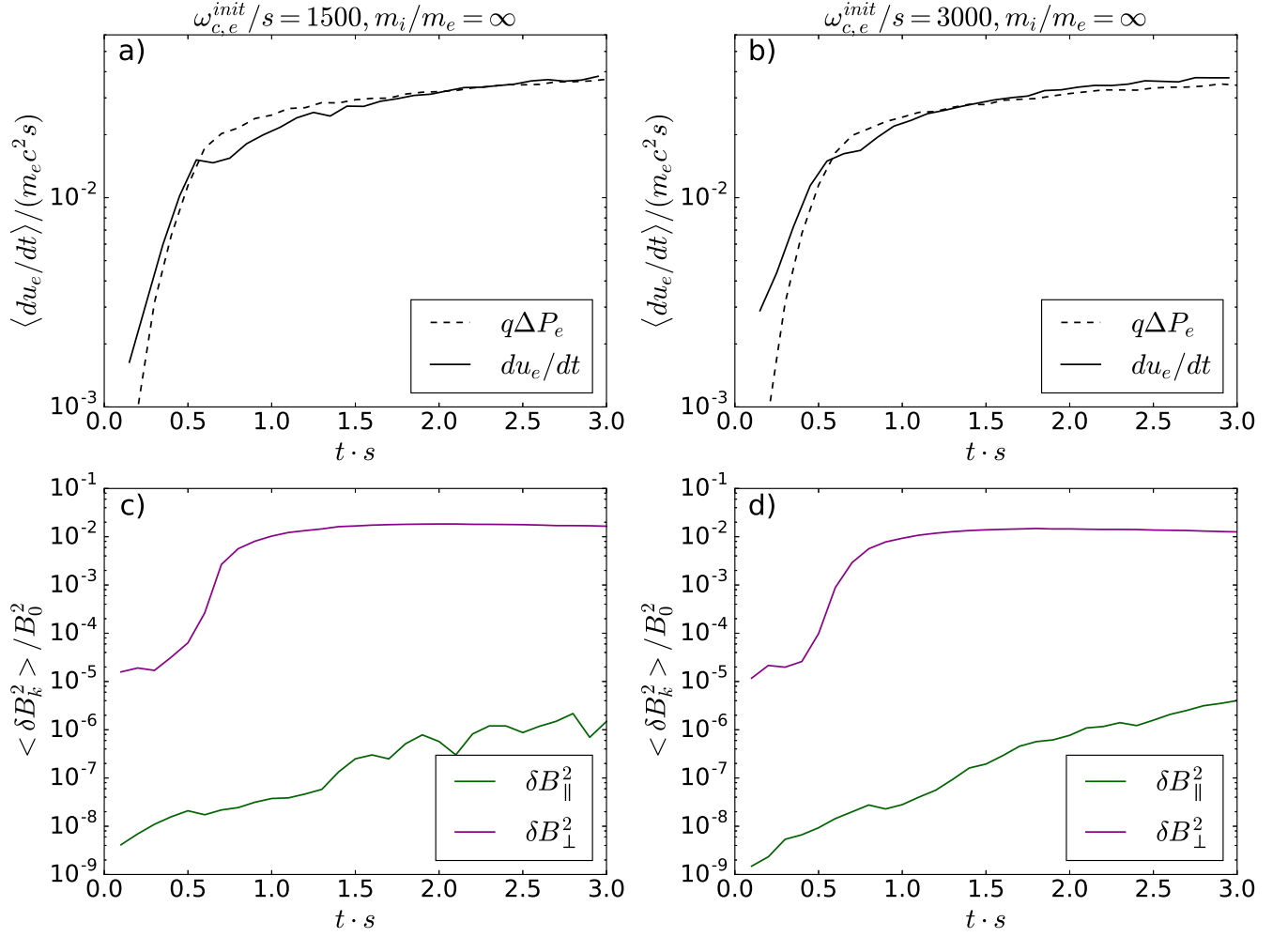


Figure 3.1: Panels *a* and *b* show the electrons heating rate for simulations OE1 ( $m_i/m_e = \infty$ , and  $\omega_{c,e}/s = 1500$ ) and OE2 ( $m_i/m_e = \infty$ , and  $\omega_{c,e}/s = 3000$ ), respectively, normalized by the electron mass energy ( $m_e c^2$ ) and shear rate ( $s$ ). Panels *c* and *d* show for the same runs the energy density in the magnetic fluctuations with direction parallel (green line) and perpendicular (magenta line) to the direction of the mean magnetic field, normalized by the initial energy density of the magnetic field ( $B_0^2/8\pi$ ).

the same temperature for ions and electrons. At the beginning of the simulations the electrons are a little more anisotropic than in the case with  $m_i/m_e = \infty$ , so the viscous heating (dashed blue line) is larger until  $t \cdot s \approx 1.5$ , where the viscous prediction reaches the same value as in the case with infinitely massive ions (dashed red line). The heating rate of the electrons is higher than the viscous prediction, by  $\sim 20\%$  and  $\sim 30\%$  for  $\omega_{c,e}^{init}/s = 1500$  and  $3000$ , respectively. In order to make sure that this is not a numerical artifact, we check energy conservation by calculating the total energy (including ions and electrons). Figures 3.2c and 3.2d show the total plasma heating rate (including both species) and compare them with their viscous prediction. It can be seen that the heating rate of the total plasma is well described by the total viscous heating. So this result implies that the discrepancy between the electrons heating rate and the viscous predictions is mainly due to the electrons taking energy from wave modes. Since these modes grow extracting their energy from the ions, they effectively work as a bridge of energy transfer between species. The fact that the transfer of energy from ions to electrons increases as  $\omega_{c,e}^{init}/s$  grows implies that, for realistic values of the magnetization, the transfer of energy from ions to electrons is likely even higher. This means that the  $\sim 20 - 30\%$  energy transfer found in our simulations should be considered as a lower limit to what would happen if realistic electron magnetizations were used.

The energy density in the magnetic fluctuations are larger than in the case where the ions have infinite mass. This is shown by the solid red and solid green lines in Figures 3.2e and 3.2f, which respectively correspond to the magnetic fluctuations perpendicular and parallel to the background magnetic field. The larger amplitude of the fluctuation in the cases with finite ion mass is a consequence of the presence of IC modes, which growth little after the whistler instability.

In simulations MR1 and MR4, the scales of the ions and electrons are, of course, poorly separated because the mass ratio is very close to unity. In order to see what is the tendency when the mass ratio between species increases, we also consider the cases  $m_i/m_e = 12$  and  $16$ .

The electron heating rate for mass ratios  $m_i/m_e = 12$  and  $16$  and  $T_i/T_e = 1$  are shown in figures 3.3a and 3.3b. For  $t \cdot s \gtrsim 1.5$ , the discrepancy between the expected heating rate due to the viscous heating and the effective heating rate reaches, for the two mass ratios,  $\sim 10\%$  and  $\sim 20\%$  for  $\omega_{c,e}^{init}/s = 1500$  and  $3000$ , respectively. Although these extra heatings are quite similar for  $m_i/m_e = 12$  and  $16$ , they are significantly smaller than for  $m_i/m_e = 4$ , specially in the case  $\omega_{c,e}^{init}/s = 3000$ . This suggest that increasing  $m_i/m_e$  has the effect of reducing the coupling between IC modes and electrons and, therefore, decreasing the transfer of energy between ions and electrons. At the same time, the role of  $\omega_{c,e}^{init}/s$  also appear to be relevant for  $m_i/m_e = 12$  and  $16$ , with the energy transfer being more significant as this parameter increases.

In order to quantify these results more accurately, Fig. 3.3c and 3.3d show the differences between the actual electron heating ( $du_e/dt$ ) and the viscous heating ( $du_e/dt/[q\Delta P_e] - 1$ ), for the same runs with finite mass ratio that we have considered before. We see that, indeed, while the relative importance of the electron energization by IC modes increases as  $\omega_{c,e}^{init}/s$  grows, this importance is reduced as  $m_i/m_e$  increases (especially in the case with  $\omega_{c,e}^{init}/s = 3000$ , but also for  $\omega_{c,e}^{init}/s = 1500$  and  $t \cdot s \gtrsim 2.5$ ).

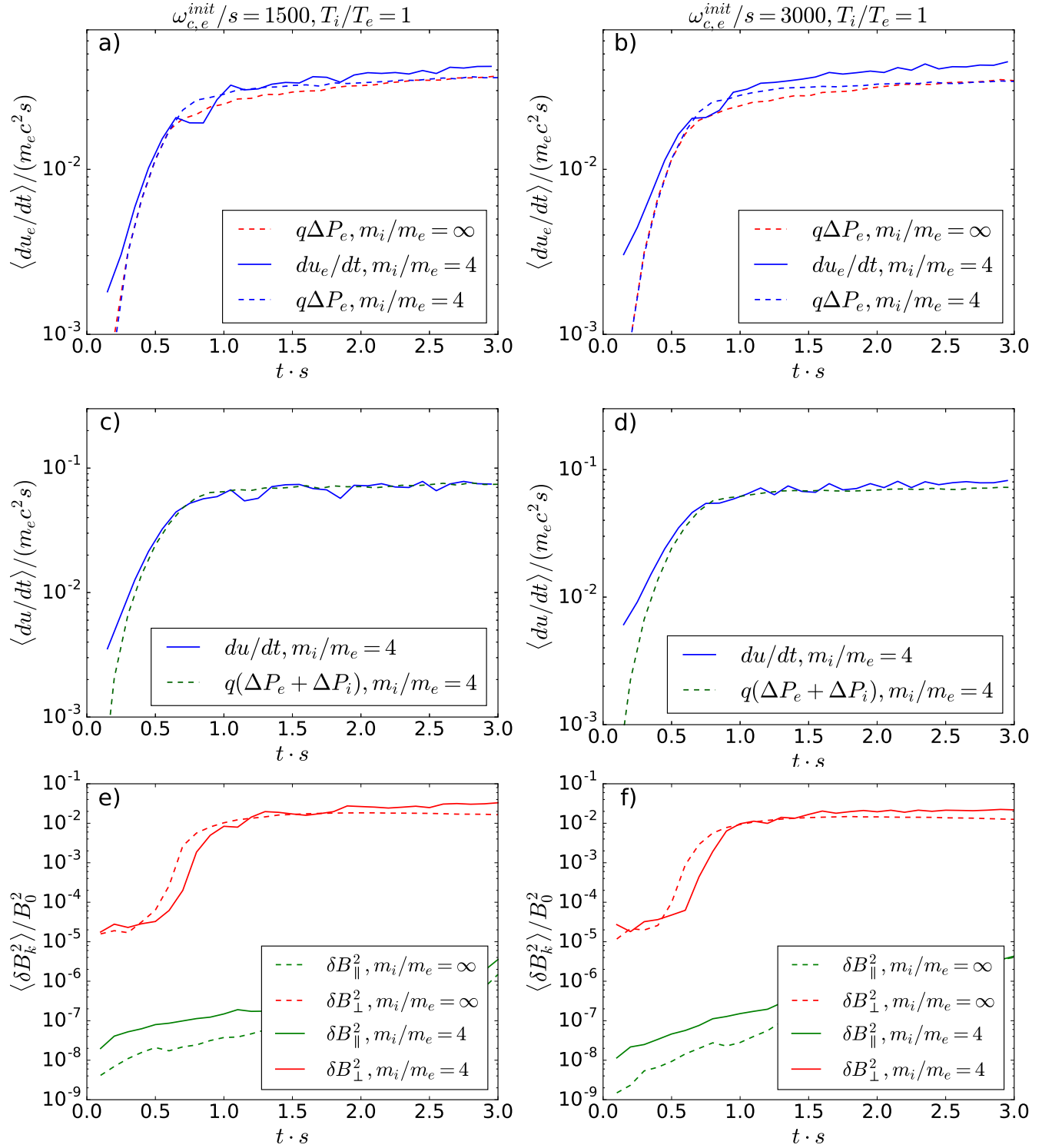


Figure 3.2: Electrons heating rate (top row) for simulations MR1 ( $m_i/m_e = 4$ , and  $\omega_{c,e}/s = 1500$ , panel *a*) and MR4 ( $m_i/m_e = 4$ , and  $\omega_{c,e}/s = 3000$ , panel *b*) normalized by the electron mass-energy ( $m_e c^2$ ) multiplied by the shear rate ( $s$ ). The plasma heating rate considering both species of particles (blue line) and the viscous heating of the total plasma (dashed green line), are shown also for runs MR1 and MR4 in panels *c* and *d*, respectively. These rate are normalized by the electron mass-energy multiplied by the shear rate. The energy density in the magnetic fluctuations with direction parallel (green line) and perpendicular (red line) to the direction of the mean magnetic field, are shown for runs MR1 and MR4 in panels *e* and *f*, respectively (and normalized by the initial magnetic energy density).

In order to make sure that the extra electron energization is not due to numerical noise, we verified that the total particle (ions + electrons) heating in the simulations with  $m_i/m_e = 12$  and 16 is well reproduced by viscous heating. Figures 3.3e and 3.3f show the total heating rate, considering both species. We see that this total heating does follows the predicted heating rate by the viscosity.

Finally, we also want to explore the heating rate of the electrons considering the same electron conditions as before ( $\beta_e^{init} = 2$ ,  $k_B T_e/m_e c^2 = 0.1$ ) but allowing the ions to be hotter with  $T_i/T_e = 3$ . The corresponding results are shown in the figures 3.4a and 3.4b. In these cases, the energy transfer from IC modes to electrons does not show significant differences between the three mass ratios analyzed ( $m_i/m_e = 4, 12$  and 16). Also, it only shows a slight increase from  $\sim 20\%$  to  $\sim 30\%$  of the heating by viscosity as  $\omega_{c,e}^{init}/s$  grows from 1500 to 3000. These percentages can be seen more clearly from Figs. 3.4c and 3.4d, which show the relative differences between the effective electron heating and the viscous heating  $(du_e/[q\Delta P_e]) - 1$ , for the same runs.

In addition, Figs.3.4e and 3.4f compare the total (ion and electron) heating with the total expected viscous heating. We see that these two quantities correspond quite well, which implies that energy is also well conserved in these runs.

In the  $T_i/T_e = 3$  case, the IC modes start growing earlier than in the case with both species having the same temperature. This is seen from Figures 3.5a and 3.5b, which show the amplitude of the magnetic fluctuations for simulations with  $\omega_{c,e}^{init}/s = 1500$  and 3000, respectively. In both cases we include simulations with  $T_i/T_e = 1$  and 3 (both with  $m_i/m_e = 16$ ) and a run with  $m_i/m_e = \infty$ . For both values of  $\omega_{c,e}^{init}/s$ , we can see that the red line, which represents the  $m_i/m_e = 16$ ,  $T_i/T_e = 1$  case, evolves very similar to the  $m_i/m_e = \infty$  case until  $t \cdot s \sim 1.2$ . After that, a second exponential growth occurs. This additional growth accounts for the effect of the mobile ions, which produce the appearance of the IC modes. The blue line (representing the case with  $m_i/m_e = 16$  and  $T_i/T_e = 3$ ), on the other hand, experiences the second exponential growth notoriously earlier than for  $T_i/T_e = 1$  (by  $t \cdot s \sim 1$ ). This earlier growth of the IC modes is because the hot ions increase the parallel beta parameter of ions ( $\beta_{\parallel,i}$ ) by a factor  $\sim 3$ , which reduces the normalized anisotropy threshold required by the ions to trigger the IC instability. Indeed, it is expected from solving the linearized Maxwell-Vlasov system that the normalized ion anisotropy necessary for triggering the IC instability with a given growth rate is given by [20, 21, 59]

$$\frac{\Delta P_j}{P_{\parallel,j}} = \frac{S_j}{\beta_{\parallel,j}^{\alpha_j}}. \quad (3.1)$$

from the literature the typical values of  $\alpha_j$  and  $S_j$  are 0.4 and 0.8, respectively.

This implies that the hotter the ions, the earlier the IC modes should appear in our simulations. Additionally, Figs 3.5a and 3.5b show that the amplitude of the IC modes increases as  $T_i/T_e$  grows. This increment in the amplitude of the fluctuations is consistent with the larger ion scattering rate necessary to maintain the ion pressure anisotropy at the lower level predicted by Eq. 3.1.

Since simulating the process of electrons energization by the IC instability using a realistic electron magnetization ( $\omega_{c,e}^{init}/s$ ) and mass ratio is out of reach for our computational capa-

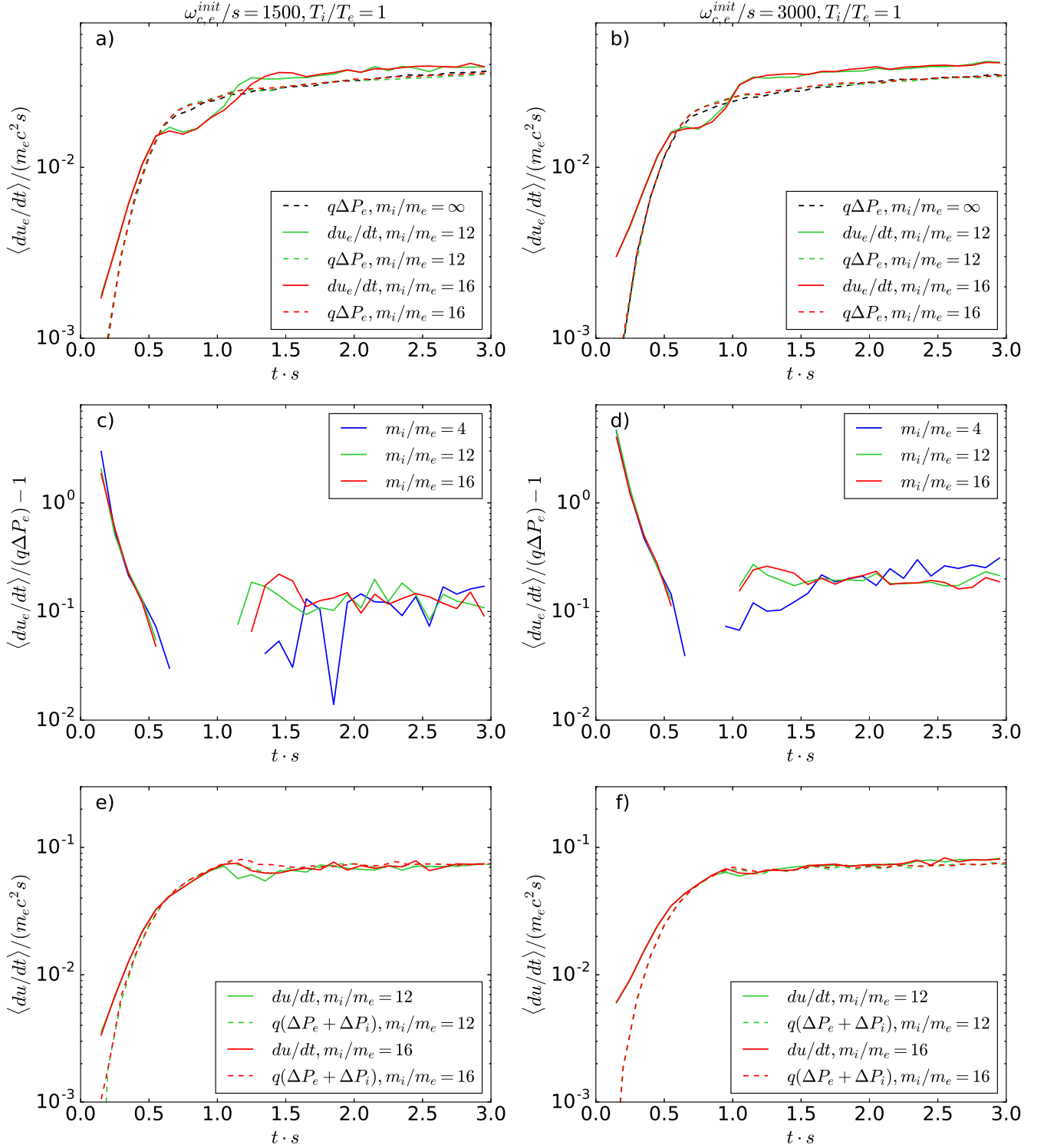


Figure 3.3: Heating rate of electrons (top row), the fractional differences between the effective electron heating and the viscous heating (middle row), and the total plasma heating rate (bottom row) for simulations with different mass ratio between ions and electrons ( $m_i/m_e = 4, 12, 16$  and  $\infty$ ) and the same temperature between species, considering two different magnetization for electrons,  $\omega_{c,e}^{init}/s = 1500$  (left column) and 3000 (right column). We compare the electrons heating rate with their predicted viscous heating (panels *a* and *b*), and quantify the fractional differences (panels *c* and *d*). And we compare the total plasma heating rate with the total plasma viscous prediction (panels *e* and *f*).

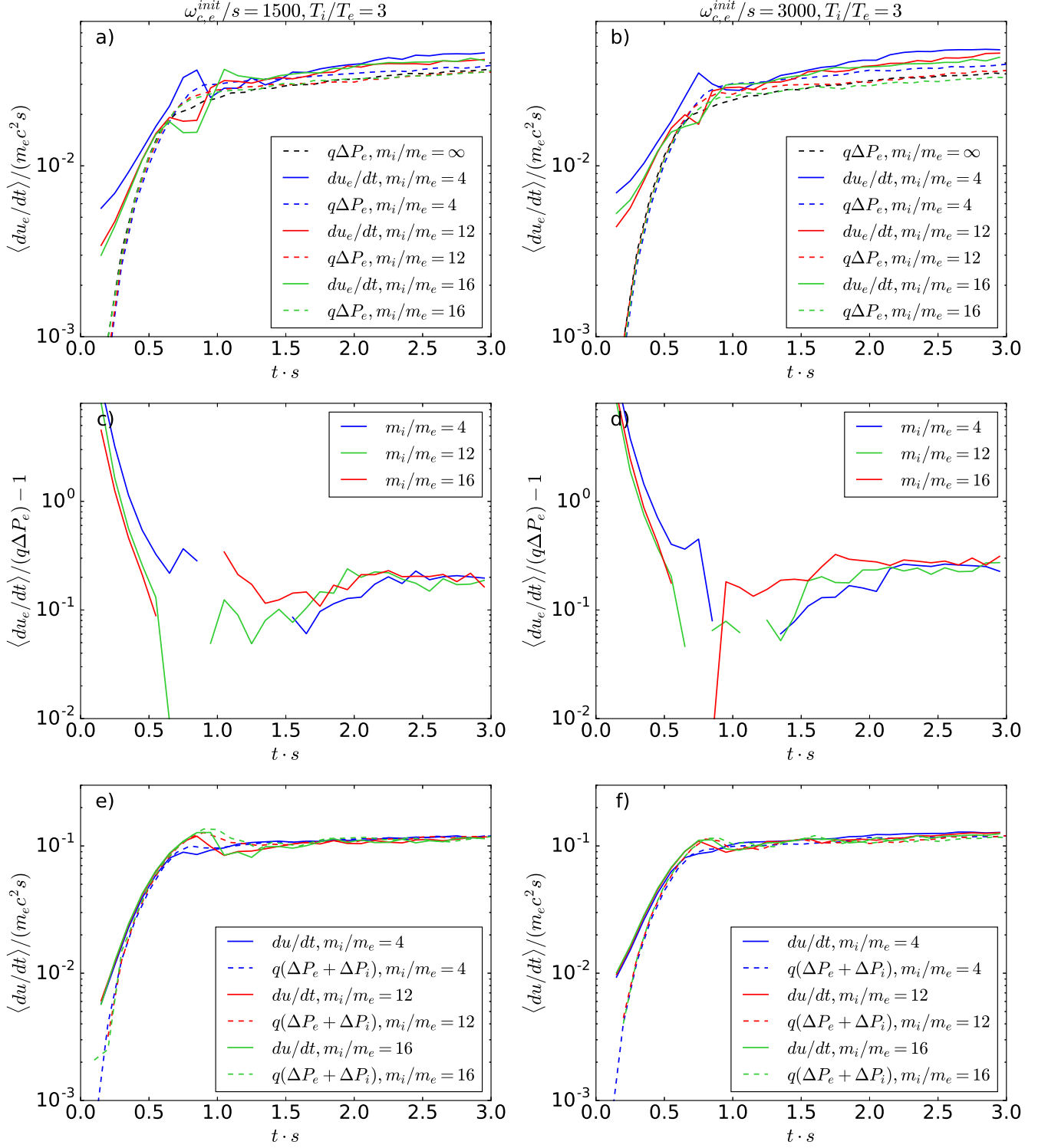


Figure 3.4: Heating rate of electrons (top row), the fractional differences between the effective electron heating and the viscous heating (middle row), and total plasma heating rate (bottom row) for simulations with different mass ratio between ions and electrons ( $m_i/m_e = 4, 12, 16$  and  $\infty$ ) and hot ions ( $T_{i0}/T_{e0} = 3$ ), considering two different magnetization for electrons,  $\omega_{c,e}^{init}/s = 1500$  (left column) and 3000 (right column). We compare the electrons heating rate with the predicted viscous heating (panels *a* and *b*), and quantify the fractional differences (panels *c* and *d*). And we compare the total plasma heating rate with the total plasma viscous prediction for the same finite mass ratio (panels *e* and *f*).

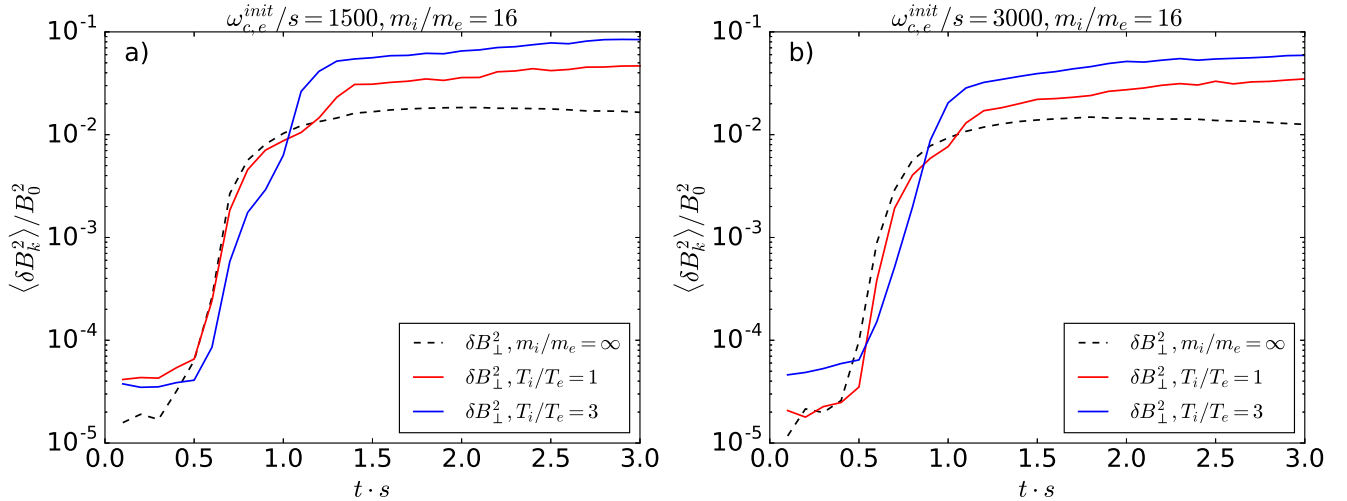


Figure 3.5: Energy density in magnetic fluctuations for simulations with mass ratio  $m_i/m_e = 16$  and temperature ratios  $T_i/T_e = 1$  (red line), and  $T_i/T_e = 3$  (blue line), compared with the case of infinitely massive ions (black dashed line), panels a) and b) correspond to magnetizations  $\omega_{c,e}^{init} = 1500$  (left) and  $\omega_{c,e}^{init} = 3000$  (right), respectively. The energy is normalized by the energy density of the initial magnetic field.

bilities, in this work we have used relatively small values of  $\omega_{c,e}^{init}/s$  and  $m_i/m_e$  in an attempt to understand the role that these parameters play in this energization. In doing so we have reached essentially two conclusions. First, as  $\omega_{c,e}^{init}/s$  grows, the electron heating by IC modes becomes more significant. Unfortunately, when testing  $\omega_{c,e}^{init}/s = 6000$  the electrons started to be heated by spurious numerical noise, in the sense that the total plasma heating was larger than the viscous prediction. This can be understood considering that, as  $s$  is decreased, the scattering rate required to limit the growth of pressure anisotropies in both ions and electrons also decreases. This means that the waves that grows in the simulations decrease their amplitude as  $s$  decreases. Therefore, at some sufficiently small value of  $s$  the electric field associated to the waves starts being smaller than the spurious electric field fluctuations associated to simulation noise, and particles start being heated by noise.

Our results thus show that the electrons heating via the interaction with IC modes triggered by the ion anisotropy could be a relevant mechanism depending on the plasma conditions.

Despite this limitation, the heating obtained from our simulations (until  $\omega_{c,e}^{init}/s = 3000$ ) can be considered as a lower limit of what should happen in a realistic astrophysical scenarios (where  $\omega_{c,e}^{init}/s$  could reach values as high as  $10^{11} - 10^{12}$  [40]).

Our second conclusion is that when  $m_i/m_e$  grows the heating of the electrons tends to decrease. (This is especially true in the case  $T_i/T_e = 1$  and  $\omega_{c,e}^{init}/s = 3000$ , and it is less clear in the other cases). This dependence on  $m_i/m_e$  can in principle be explained by the separation of temporal and spatial scales that characterized the ion and electron dynamics. This will be explained in detail in Section 3.3, where we will present a simple model that will allow us to understand these results and to speculate about what should happen in realistic astrophysical plasmas. However, before that, we will describe the effect that the observed electron energization by IC modes has on the energy spectrum of the electrons.

## 3.2 Electron acceleration

In the same way as before, we will use the simulations with infinitely massive ions as reference, so that we can separate the effect of the IC modes from the one of the whistler waves, which have been found to also produce non-thermal features in the electron spectra [42].

In this section we will analyze the energy spectrum of electrons at the end of the simulations for different mass ratios  $m_i/m_e = 4, 12, 16$  and  $\infty$ , and for  $T_i/T_e = 1$  and 3. This analysis is intended to compare the relevance of ions in the formation of non-thermal components of electrons, especially considering scenarios where the electron energization by IC modes is significant.

In order to test the importance of magnetization, in the figure 3.6 we compare the spectra of simulations with infinitely massive ions and with electron magnetizations magnetization  $\omega_{c,e}^{init} = 1500$  and 3000. We see that the distribution in the higher magnetization case slightly hardens the high energy tail, but it is basically the same as that formed in the less magnetized case. This confirms the results of [42], which shows that in these scenarios (ignoring the dynamics of the ions), increasing the magnetization does not have a significant impact on the formation of the non-thermal tail.

Figure 3.7a shows the energy distribution of the electrons for the runs MR1, MR2, MR3 and OE1 ( $\omega_{c,e}^{init} = 1500$ ,  $T_i/T_e = 1$ , and  $m_i/m_e = 4, 12, 16$  and  $\infty$ , respectively). These simulations show that the spectral index of the high energy tail is not significantly affected for moderately large mass ratios ( $m_i/m_e \gtrsim 12$ ), while for smaller mass ratios the electrons show a much harder non-thermal component. Figure 3.7b shows the energy spectrum of the electrons reached at the end of the simulations, for the runs MR4, MR5, MR6 and OE2 ( $\omega_{c,e}^{init} = 3000$ ,  $T_i/T_e = 1$  and  $m_i/m_e = 4, 12, 16$  and  $\infty$ , respectively). In the same way as in Fig. 3.7a the spectral index obtained for the case with infinitely massive ions reproduces quite well in simulations with  $m_i/m_e \geq 12$ .

In both panels of Fig 3.7 the high-energy tail becomes significantly harder when  $m_i/m_e = 4$ . Considering that the energy transfer from the IC modes to the electron for  $m_i/m_e = 4$  appears to be larger than in the  $m_i/m_e = 12$  and 16 cases, this suggests the extra electron energization by IC waves is indeed non-thermal.

Nevertheless, in both panels of the figure 3.7 it is shown that the effect that ions have in the spectrum does not depend on the plasma magnetization ( $\omega_{c,e}/s$ ). Even for simulations with  $m_i/m_e = 4$  the increase of the non-thermal component in the distribution is fairly independent of  $\omega_{c,e}^{init}/s$ . This is consistent with the fact that, for the  $T_i/T_e = 1$  runs, the most efficient energy transfer occurs for the two cases with  $m_i/m_e = 4$ , and depends weakly on  $\omega_{c,e}^{init}/s$ .

Panels a and b in Fig. 3.8 show the electron spectrum reached at the end of simulations with hottest ions ( $T_i/T_e = 3$ ), when  $\omega_{c,e}^{init}/s = 1500$  (Fig. 3.8a) and  $\omega_{c,e}^{init}/s = 3000$  (Fig. 3.8b), for different mass ratios. We see that for this value of  $T_i/T_e$ , the difference with the  $m_i/m_e = \infty$  case are less significant than for the  $T_i/T_e = 1$  case. These differences, however, are still somewhat more important for  $m_i/m_e = 4$  and decrease as  $m_i/m_e$  grows. In addition, the

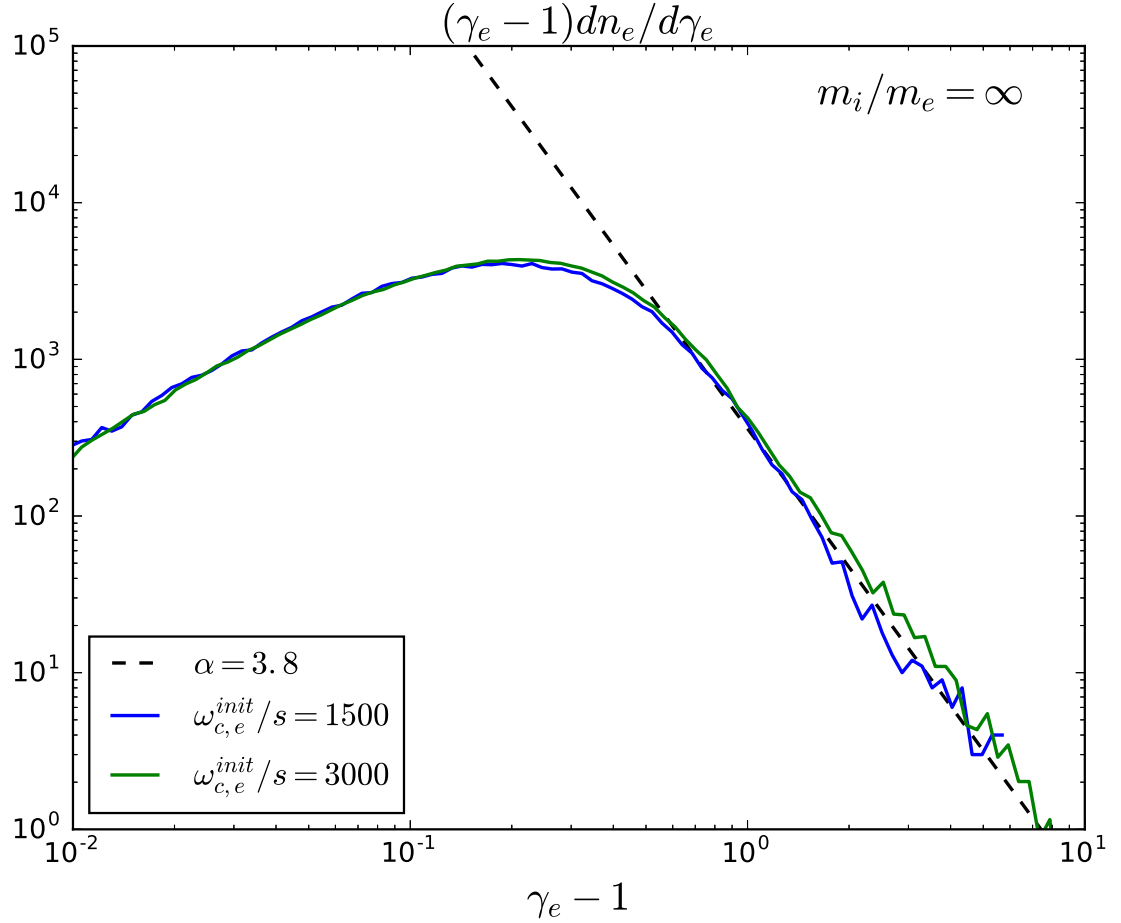


Figure 3.6: Electron energy distribution reached at the end of the simulations. The blue line shows the result of the simulation OE1 ( $m_i/m_e = \infty$ ,  $\omega_{c,e}^{init} = 1500$ ). The green line shows the simulation OE2 ( $m_i/m_e = \infty$ ,  $\omega_{c,e}^{init} = 3000$ ), and the black dashed line shows the fitting of the high energy tail, which follows a power law type distribution with spectral index  $\alpha \sim 3.8$ .

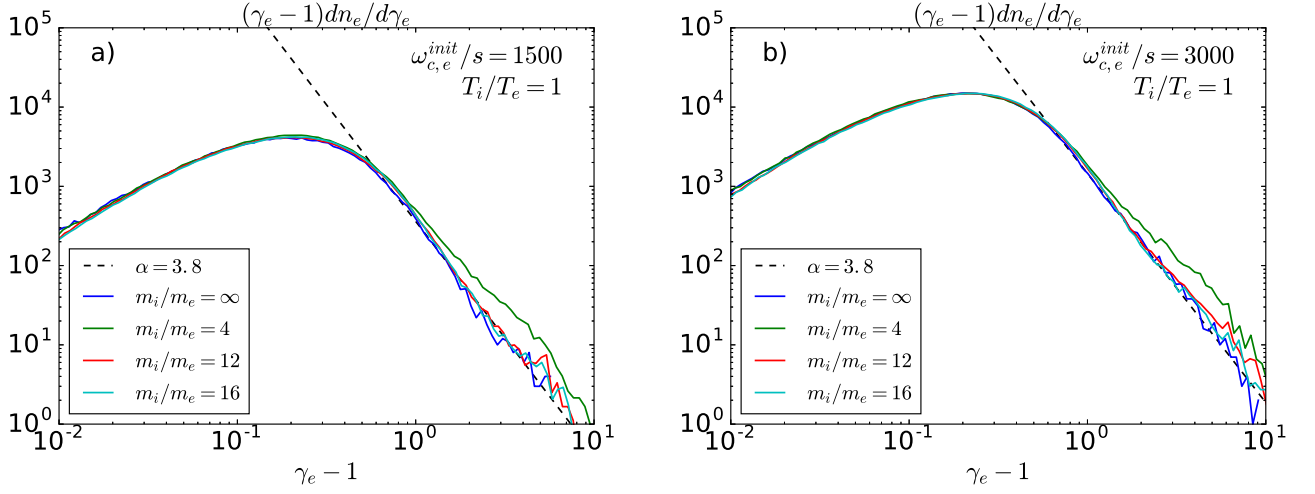


Figure 3.7: The final electron spectra ( $t \cdot s = 3$ ) for simulation with the same parameters  $k_B T_e = 0.1 m_e c^2$ ,  $T_i/T_e = 1$ ,  $\beta_e^{init} = 2$ . The runs in panel a) have  $\omega_{c,e}^{init} = 1500$  and  $m_i/m_e = 4, 12, 16$  and  $\infty$  (runs MR1, MR2, MR3 and OE1, respectively). The runs in panel b) have  $\omega_{c,e}^{init} = 3000$  and  $m_i/m_e = 4, 12, 16$  and  $\infty$  (runs MR4, MR5, MR6 and OE2, respectively).

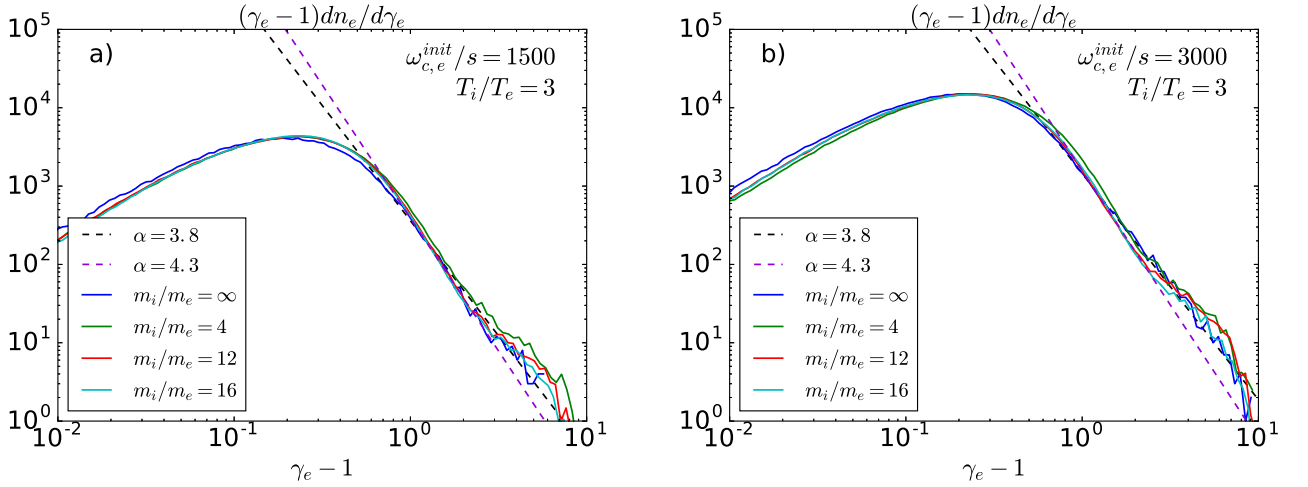


Figure 3.8: The final electron spectra ( $t \cdot s = 3$ ) for simulation with the same parameters  $k_B T_e = 0.1 m_e c^2$ ,  $T_i/T_e = 3$ ,  $\beta_e^{init} = 2$ . The runs in panel a) have  $\omega_{c,e}^{init} = 1500$  and  $m_i/m_e = 4, 12, 16$  and  $\infty$  (runs TR1, TR2, TR3 and OE1, respectively). The runs in panel b) have  $\omega_{c,e}^{init} = 3000$  and  $m_i/m_e = 4, 12, 16$  and  $\infty$  (runs TR4, TR5, TR6 and OE2, respectively).

magnetization does not appear to play an important role.

These results for  $T_i/T_e = 3$  are consistent with the weaker dependence of the extra electron heating on  $m_i/m_e$  and  $\omega_{c,e}^{init}/s$  observed in §3.1. This confirms the qualitative result that the heating of electrons by IC waves produces significant non-thermal features in the electron spectrum and, therefore, these features are more prominent in the cases where the heating is more significant.

As we explained above, the ability of the ions to render the IC modes unstable relies on their capacity to resonate with these modes. Similarly, a reasonable requirement for the efficient transfer of energy from the IC modes to the electrons is for the latter to also be able to resonate with the IC modes. In the next section we argue that this resonance condition is most likely one of the main factors in determining the efficiency of this energy transfer in our simulations. After that, we also speculate about the astrophysical plasma conditions where we expect this energy transfer to be significant.

### 3.3 Discussion

In this section we show that the energy transfer from IC modes to the electrons can be explained in terms of the resonance condition between the electrons and the IC modes. Without loss of generality, we assume that the waves propagate parallel to a background magnetic field  $\mathbf{B} = B\hat{b}$  ( $B > 0$ ). Thus, the resonance condition between particles “ $j$ ” and the left-handed polarized IC waves is:

$$\frac{\omega}{k} - v_{j,\parallel} = \frac{\omega_{c,j}}{k\gamma_j}, \quad (3.2)$$

where  $\omega$  and  $k$  are the frequency and the wave number of the waves, respectively (we assume  $\omega > 0$  and  $k > 0$  or  $< 0$  to allow different direction of propagation for the modes). In addition,  $v_{j,\parallel}$ ,  $\omega_{c,j}$  and  $\gamma_j$  are the velocity parallel to  $\mathbf{B}$ , the non-relativistic cyclotron frequency ( $q_j B/m_j c$ ) and the Lorentz factor of the particles, respectively.

Considering that  $\omega_{c,e} < 0$ , Equation 3.2 implies that the resonance with the electrons requires these particles to move in the same direction and faster than the IC waves ( $|v_{e,\parallel}| > |\omega/k|$ ), regardless of whether  $k > 0$  or  $< 0$ .

The requirement  $|v_{e,\parallel}| > |\omega/k|$  is easily achieved in a plasma with  $\beta_e^{init} \sim \beta_i^{init} \sim 1$  (which means  $T_i \sim T_e$ ). Indeed, we know that the phase velocity of the IC modes satisfies  $|\omega/k| \lesssim c\omega_{c,i}/\omega_{p,i}$  [14]. Thus, in order to resonate with the IC modes, the electrons need to move faster than  $c\omega_{c,i}/\omega_{p,i}$ . However, we know that

$$\beta_i^{init} = 2(k_B T_i/m_i)/(c\omega_{c,i}/\omega_{p,i})^2, \quad (3.3)$$

which, given that  $\beta_i^{init} \sim 1$ , means that  $|v_{e,\parallel}| > c\omega_{c,i}/\omega_{p,i}$  is satisfied if the electrons move faster than  $(k_B T_i/m_i)^{1/2}$ . However, a reasonable estimate for  $v_{e,\parallel}$  of the electrons is their

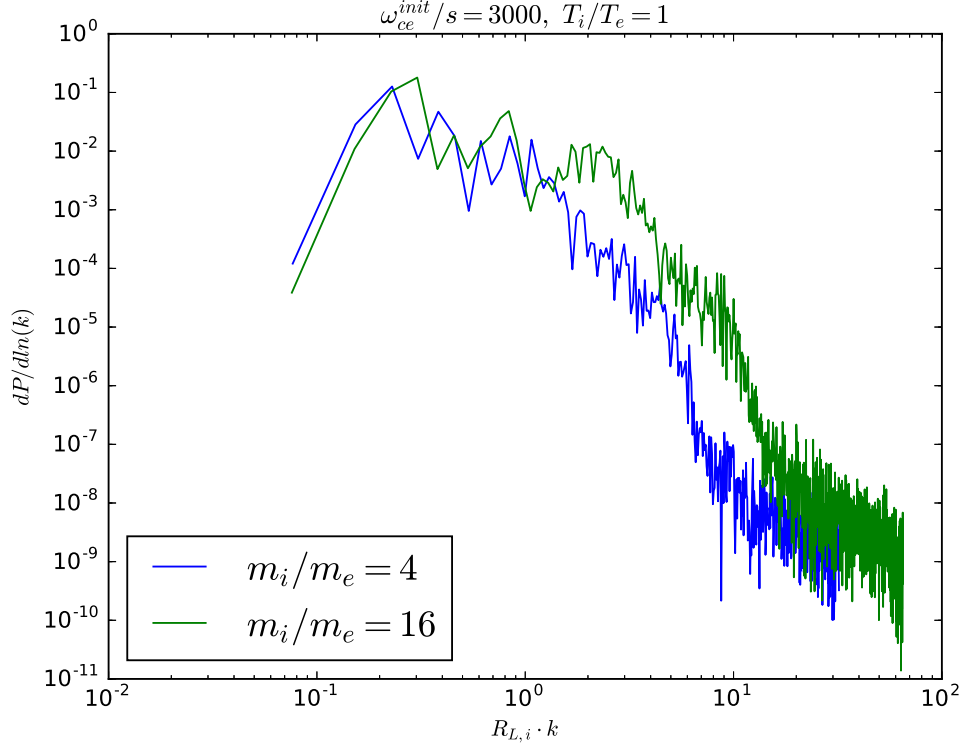


Figure 3.9: Power spectrum of magnetic field fluctuations, both lines have electrons in the same conditions,  $\omega_{ce}^{init}/s = 3000$  and  $\beta_e^{init} = 2$ , but with different mass ratios between ions and electrons  $m_i/m_e = 4$  and  $12$ , in blue and green, respectively.

“thermal velocity”  $(k_B T_e/m_e)^{1/2}$ , which is indeed significantly larger than  $(k_B T_i/m_i)^{1/2}$  provided that  $T_i \sim T_e$  and that  $m_i/m_e$  is larger than 1. It is important to notice, however, that this analysis is valid for non-relativistic electrons. When electrons are relativistic,  $v_{e,\parallel} \sim c$  and the resonance condition simply requires for  $\omega_{c,i}/\omega_{p,i}$  to be smaller than 1, which is a reasonable expectation for the inner regions of accretion flows around black holes.

Thus assuming that  $|v_{e,\parallel}|$  is significantly larger than  $|\omega/k|$ , Equation 3.2 can be approximated to

$$|v_{e,\parallel}| \approx \left| \frac{\omega_{c,e}}{k\gamma_e} \right|. \quad (3.4)$$

If in addition we make the reasonable assumption that  $|v_{\parallel}\gamma_e|$  is of the order of  $c(k_B T_e/m_e)^{1/2}$  (which is valid both in the relativistic and non-relativistic regimes), the resonant condition simply becomes:

$$k \approx \frac{1}{R_{L,e}^r}, \quad (3.5)$$

where  $R_{L,e}^r$  is the *relativistic* Larmor radius of the electrons (i.e., it includes the possibility for  $\gamma_e$  to be significantly larger than 1).

Thus, using Equation 3.5 we can estimate the plasma conditions that could optimize the

transfer of energy from the IC waves to the electrons. For this we consider the well known result that the IC instability preferentially amplifies waves with wave numbers  $k$  close to  $1/R_{L,i}^r$ , where  $R_{L,i}^r$  is the Larmor radius of the ions. This is verified in our simulations considering the power spectra of runs MR4 and MR6, which use the same electron conditions but different values of  $m_i/m_e$ . These spectra are shown in Figure 3.9 for  $t \cdot s = 2$ , and show that most of the power produced by the IC appears at a fixed value of  $kR_{L,i}^r$  ( $\approx 0.3$ ), regardless of the value of  $m_i/m_e$ . Considering this property of the wave number of the most unstable IC modes, we conclude that the transfer of energy from the IC modes to the electrons should be maximized in plasmas where

$$R_{L,e}^r \approx 3R_{L,i}^r. \quad (3.6)$$

Equation 3.6 naturally explains why in our simulations with  $T_i/T_e = 1$  the transfer of energy to the electrons is maximized for  $m_i/m_e = 4$  and it significantly decreases in the cases  $m_i/m_e = 12$  and  $16$ . Indeed, as  $m_i/m_e$  decreases, the ion and electron Larmor radii become more similar, easing the resonant interaction between the electrons and the IC waves. Equation 3.6 also explains the decrease in this energy transfer in the case  $m_i/m_e = 4$  when  $T_i/T_e$  grows from 1 to 3. In that case, the difference between  $R_{L,i}^r$  and  $R_{L,e}^r$  increases, making the resonance harder. However, the smaller difference between mass ratios  $m_i/m_e = 4, 12$  and  $16$  is not consistent with the increase in the separation between  $R_{L,i}^r$  and  $R_{L,e}^r$  as  $m_i/m_e$  grows. This indicates that other factors, apart from the resonance condition alone are probably playing a role as well. For instance, the scattering frequency  $\nu_{sc}$  of ions due to their resonance with IC modes is expected to scale as

$$\nu_{sc} \sim \omega_{c,i} \delta B^2 / B^2, \quad (3.7)$$

where  $\delta B/B$  is the amplitude of the IC modes normalized by the background magnetic field [42]. In our simulations  $\nu_{sc}$  must be of the order of the shear rate of the plasma,  $s$ . This is simply because the scattering rate of the ions must be close to the rate at which their pressure anisotropy growth is driven, so that there is a nearly stationary behavior of the anisotropy. Thus, given Equation 3.7, when the electrons interact resonantly with the IC modes their scattering frequency should be  $\propto s m_i/m_e$  (since  $\omega_{c,e}/\omega_{c,i} = m_i/m_e$ ). This implies that, although increasing  $m_i/m_e$  may reduce the extent to which the electrons are resonantly scattered by the IC waves, the decrease in the corresponding scattering frequency may not be so substantial due to the way this frequency scales with the cyclotron frequency of the particles.

Despite these considerations, our results suggest that the energy transfer from IC modes to the electrons is significantly influenced by the ability of the electrons to resonate with these waves. This requirement implies that significant transfer of energy is expected in cases where the electrons have Larmor radii comparable to the one of the ions. Although this transfer of energy is probably  $\sim 10\%$  of the electron heating due to anisotropic viscosity, our results show that it should affect the electrons “non-thermally”, in the sense that it would mainly modify the high energy part of the electron energy spectra. In the next section we discuss astrophysical scenarios where this “non-thermal” transfer of energy can occur.

# Summary and Conclusion

In this Master's thesis, we used particle-in-cell (PIC) plasma simulations to study the possible electron energization by ion-cyclotron (IC) waves in a collisionless plasma. Although these types of plasmas are ubiquitous in astrophysics, our main motivation is given by the accretion disk of the supermassive black hole Sagittarius A\* (Sgr A\*) at the center of the Milky Way. This system is currently being observed by state-of-the-art experiments, which in the very near future are expected to obtain images of the accreting system, attaining angular resolutions comparable to the event horizon of the black hole (e.g., the Event Horizon Telescope in radio [32] and GRAVITY in infrared [1]). Although these experiments constitute a marvelous opportunity to test gravity under the most extreme conditions, their success requires a complete and detailed understanding of the plasma physics of the accretion disk in Sgr A\*. In particular, parameters like the electron temperature and electron energy spectrum are crucial to correctly predict the images that these types of experiments will observe at different wavelengths (see, e.g., [10]).

The goal of this thesis was to study one particular channel through which the electrons can get energized in collisionless accreting systems. This is the possible interaction of the electrons with IC waves. These waves are believed to be produced by the so-called IC instability, which is driven by the ion pressure anisotropy expected due to ion magnetic moment conservation. Since the IC waves obtain their energy mainly from the ions, this mechanism, if effective, has the potential to constitute a way for the ions to transfer part of their energy to electrons, even in the absence of Coulomb collisions.

This potential energy transfer has been previously claimed by [50, 49] in the context of collisionless accretion disks. However, these works consider the case in which  $T_e/T_i < 0.2$  (where  $T_e$  and  $T_i$  are the electron and ion temperatures), and only focus on the exponential growth stage of the IC instability. As we argue above, this exponential regime is only a transient that does not represent what happens in the disk most of the time, given that the magnetic field should mainly grow as the plasma is accreted onto the central black hole. Also, given that the ratio  $T_e/T_i$  is unknown, it is important to consider this possible energy transfer in the regime  $T_e/T_i \sim 1$ . Because of this, the goal of this thesis is to extend the work of [50, 49] to the non-linear, saturated regime of the IC instability, and to consider cases where  $T_e/T_i \sim 1$ .

In order to attain the nonlinear regime of the IC modes, we used shearing simulations where the ion and electron pressure anisotropies were driven for times longer than the exponential growth regime of the IC instability. In this case, the main expected electron heating mech-

anism is anisotropic viscosity (see Eq. D.3). Thus our way to quantify the importance of the possible electron energization by IC modes was by comparing it with the viscous heating.<sup>2</sup> Since the relevant instabilities for this study involve modes that are parallel to the background magnetic field, we used computationally cheap 1D simulations. The suitability of these simulations was successfully tested in §2, by comparing them with analogous 2D simulations where the IC and whistler instabilities dominate.<sup>3</sup>

One important challenge in our study was that our runs cannot reach realistic values for the quantities  $\omega_{c,e}^{init}/s$  and  $m_i/m_e$ . Thus, although in realistic astrophysical cases these parameters have relatively well defined values, we treated them as free parameters with the aim of understanding the effect that they have in the energization of electrons by the IC modes.

Our simulation strategy was thus to limit the electron conditions to:  $k_B T_e/m_e c^2 = 0.1$  and  $\beta_e^{init} = 2$  (relevant for the inner regions of low collisionality accretion flows around black holes), and vary their magnetization using two values:  $\omega_{c,e}^{init}/s = 1500$  and  $3000$ . Then, after fixing these conditions for the electrons, we vary the ion conditions using  $m_i/m_e = 4, 12$  and  $16$  and  $T_i/T_e = 1$  and  $3$ .

In all the cases considered, our simulations showed an electron energization by IC modes that is  $\sim 10 - 20\%$  of the expected electron heating from anisotropic viscosity. This implies that, as a mere source of energy, the interaction between the electrons and the IC modes does not appear to be significant. However, the observed energization appears to be “non-thermal”, in the sense that it mainly enhances the high energy tail of the electron spectrum. The extra energization tends to increase a little when increasing  $\omega_{c,e}^{init}/s$ , but in a rather weak way, so in our view it is unlikely that using realistic values of  $\omega_{c,e}^{init}/s$  would considerably change this scenario. But perhaps most importantly, there is a dependence on  $m_i/m_e$  that makes the transfer of energy increase as  $m_i/m_e$  decreases. As we mentioned in §3, this trend is consistent with the fulfillment of the resonance condition between electrons and IC waves, which implies that the typical electron (relativistic) Larmor radius needs to be close to the corresponding ion Larmor radius (Eq. 3.6).

While in a plasma with a realistic value of  $m_i/m_e$  this requirement may be difficult to attain, there are some cases where Eq. 3.6 could be satisfied. In fact, in the sub-relativistic plasma regime of systems like Sgr A\*, where  $m_e c^2 \ll k_B T_e \sim k_B T_i < m_i c^2$  (see, e.g., [9]) one can show that

$$R_{L,e}^r/R_{L,i}^r \approx (k_B T_i/m_i c^2)^{1/2}. \quad (3.8)$$

Thus, if  $(k_B T_i/m_i c^2)^{1/2}$  is, say,  $\sim 1/5$ , as expected in the inner region of Sgr A\* accretion flow [9], some electrons with energies  $\sim 5$  times larger than the ones of the thermal part of their energy spectrum could in principle resonate with IC waves. These pre-accelerated electrons could be easily achieved by other processes that may operate in the sub-relativistic regime of weakly collisional accretion flows. These include stochastic acceleration by whistler waves

---

<sup>2</sup>This is of course keeping in mind that there are other potentially important heating mechanisms, as mentioned in the Introduction.

<sup>3</sup>Notice that the validity of this method was also tested in [31], in a study dedicated to ion acceleration by the IC instability.

[42], magnetic reconnection [6, 58], and the damping of MHD turbulence [62]. The possibility of (pre-accelerated) non-thermal electron being further energized by IC modes in the context of a sub-relativistic collisionless plasma will be explored in a future investigation.

# Bibliography

- [1] R. Abuter, A. Amorim, M. Bauböck, J. Berger, H. Bonnet, W. Brandner, Y. Clénet, V. C. du Foresto, P. de Zeeuw, C. Deen, et al. Detection of orbital motions near the last stable circular orbit of the massive black hole sgra. *Astronomy & Astrophysics*, 618:L10, 2018.
- [2] B. Anderson, S. Fuselier, and D. Murr. Electromagnetic ion cyclotron waves observed in the plasma depletion layer. *Geophysical research letters*, 18(11):1955–1958, 1991.
- [3] F. Baganoff, M. Bautz, W. N. Brandt, G. Chartas, E. Feigelson, G. Garmire, Y. Maeda, M. Morris, G. Ricker, L. Townsley, et al. Rapid X-ray flaring from the direction of the supermassive black hole at the galactic centre. *Nature*, 413(6851):45, 2001.
- [4] F. K. Baganoff, Y. Maeda, M. Morris, M. Bautz, W. Brandt, W. Cui, J. Doty, E. Feigelson, G. Garmire, S. Pravdo, et al. Chandra X-ray spectroscopic imaging of sagittarius A\* and the central parsec of the galaxy. *The Astrophysical Journal*, 591(2):891, 2003.
- [5] S. A. Balbus and J. F. Hawley. A powerful local shear instability in weakly magnetized disks. i-linear analysis. ii-nonlinear evolution. *The Astrophysical Journal*, 376:214–233, 1991.
- [6] D. Ball, L. Sironi, and F. Özel. Electron and proton acceleration in trans-relativistic magnetic reconnection: Dependence on plasma beta and magnetization. *The Astrophysical Journal*, 862(1):80, jul 2018.
- [7] C. K. Birdsall and A. B. Langdon. *Plasma physics via computer simulation*. CRC press, 2004.
- [8] O. Buneman. *Computer space plasma physics, simulation techniques and software* ed h. matsumoto and y. omura, 1993.
- [9] A. Chael, M. Rowan, R. Narayan, M. Johnson, and L. Sironi. The role of electron heating physics in images and variability of the galactic centre black hole sagittarius A\*. *Monthly Notices of the Royal Astronomical Society*, 2018.
- [10] A. A. Chael, R. Narayan, and A. Sadowski. Evolving non-thermal electrons in simulations of black hole accretion. *Monthly Notices of the Royal Astronomical Society*, 470(2):2367–2386, 2017.

- [11] A. Y. Chen and A. M. Beloborodov. Electrodynamics of axisymmetric pulsar magnetosphere with electron-positron discharge: a numerical experiment. *The Astrophysical Journal Letters*, 795(1):L22, 2014.
- [12] C.-Z. Cheng and G. Knorr. The integration of the vlasov equation in configuration space. *Journal of Computational Physics*, 22(3):330–351, 1976.
- [13] G. Chew, M. Goldberger, and F. Low. The Boltzmann equation and the one-fluid hydromagnetic equations in the absence of particle collisions. *Proc. R. Soc. Lond. A*, 236(1204):112–118, 1956.
- [14] J. M. Cornwall and M. Schulz. Electromagnetic ion-cyclotron instabilities in multicomponent magnetospheric plasmas. *Journal of Geophysical Research*, 76(31):7791–7796, 1971.
- [15] J. Dudík, M. Janvier, G. Aulanier, G. Del Zanna, M. Karlický, H. E. Mason, and B. Schmieder. Slipping magnetic reconnection during an x-class solar flare observed by sdo/aia. *The Astrophysical Journal*, 784(2):144, 2014.
- [16] N. V. Elkina and J. Büchner. A new conservative unsplit method for the solution of the Vlasov equation. *Journal of Computational Physics*, 213(2):862–875, 2006.
- [17] E. Fermi. On the origin of the cosmic radiation. *Physical Review*, 75(8):1169, 1949.
- [18] S. P. Gary. The mirror and ion cyclotron anisotropy instabilities. *Journal of Geophysical Research: Space Physics*, 97(A6):8519–8529, 1992.
- [19] S. P. Gary. *Theory of space plasma microinstabilities*. Cambridge university press, 2005.
- [20] S. P. Gary and H. Karimabadi. Linear theory of electron temperature anisotropy instabilities: Whistler, mirror, and weibel. *Journal of Geophysical Research: Space Physics*, 111(A11), 2006.
- [21] S. P. Gary and J. Wang. Whistler instability: Electron anisotropy upper bound. *Journal of Geophysical Research: Space Physics*, 101(A5):10749–10754, 1996.
- [22] V. Génot, S. Schwartz, C. Mazelle, M. Balikhin, M. Dunlop, and T. Bauer. Kinetic study of the mirror mode. *Journal of Geophysical Research: Space Physics*, 106(A10):21611–21622, 2001.
- [23] S. Gillessen, F. Eisenhauer, S. Trippe, T. Alexander, R. Genzel, F. Martins, and T. Ott. Monitoring stellar orbits around the massive black hole in the galactic center. *The Astrophysical Journal*, 692(2):1075, 2009.
- [24] P. Goldreich and S. Sridhar. Toward a theory of interstellar turbulence. 2: Strong alfvénic turbulence. *The Astrophysical Journal*, 438:763–775, 1995.
- [25] H. Goldstein. *Classical mechanics*. Pearson Education India, 2011.

- [26] D. A. Gurnett and A. Bhattacharjee. *Introduction to Plasma Physics: With Space and Laboratory Applications*. Cambridge University Press, 2005.
- [27] A. Hasegawa. Drift mirror instability in the magnetosphere. *The Physics of Fluids*, 12(12):2642–2650, 1969.
- [28] G. G. Howes. A prescription for the turbulent heating of astrophysical plasmas. *Monthly Notices of the Royal Astronomical Society: Letters*, 409(1):L104–L108, 2010.
- [29] A. Koratkar and O. Blaes. The ultraviolet and optical continuum emission in active galactic nuclei: the status of accretion disks. *Publications of the Astronomical Society of the Pacific*, 111(755):1, 1999.
- [30] R. Kulsrud. Basic plasma physics. *Handbook of plasma physics*, 1, 1983.
- [31] F. Ley, M. Riquelme, L. Sironi, D. Verscharen, and A. Sandoval. Stochastic Ion Acceleration by the Ion-cyclotron Instability in a Growing Magnetic Field. *arXiv e-prints*, page arXiv:1903.11238, Mar 2019.
- [32] R.-S. Lu, T. P. Krichbaum, A. L. Roy, V. L. Fish, S. S. Doeleman, M. D. Johnson, K. Akiyama, D. Psaltis, W. Alef, K. Asada, et al. Detection of intrinsic source structure at 3 schwarzschild radii with millimeter-vlbi observations of sagittarius A\*. *The Astrophysical Journal*, 859(1):60, 2018.
- [33] J. W. Lynn, I. J. Parrish, E. Quataert, and B. D. G. Chandran. Resonance broadening and heating of charged particles in magnetohydrodynamic turbulence. *The Astrophysical Journal*, 758(2):78, sep 2012.
- [34] J. W. Lynn, E. Quataert, B. D. G. Chandran, and I. J. Parrish. Acceleration of relativistic electrons by magnetohydrodynamic turbulence: implications for non-thermal emission from black hole accretion disks. *The Astrophysical Journal*, 791(1):71, jul 2014.
- [35] R. Mahadevan and E. Quataert. Are particles in advection-dominated accretion flows thermal? *The Astrophysical Journal*, 490(2):605, 1997.
- [36] M. McQuinn. The evolution of the intergalactic medium. *Annual Review of Astronomy and Astrophysics*, 54:313–362, 2016.
- [37] R. Narayan and I. Yi. Advection-dominated accretion: underfed black holes and neutron stars. *arXiv preprint astro-ph/9411059*, 1994.
- [38] S. Ossakow, I. Haber, and E. Ott. Simulation of whistler instabilities in anisotropic plasmas. *The Physics of Fluids*, 15(8):1538–1540, 1972.
- [39] E. N. Parker. Sweet’s mechanism for merging magnetic fields in conducting fluids. *Journal of Geophysical Research*, 62(4):509–520, 1957.
- [40] G. Ponti, E. George, S. Scaringi, S. Zhang, C. Jin, J. Dexter, R. Terrier, M. Clavel, N. Degenaar, F. Eisenhauer, et al. A powerful flare from sgr A\* confirms the syn-

- chrotron nature of the X-ray emission. *Monthly Notices of the Royal Astronomical Society*, 468(2):2447–2468, 2017.
- [41] E. Quataert and A. Gruzinov. Turbulence and particle heating in advection-dominated accretion flows. *The Astrophysical Journal*, 520(1):248, 1999.
- [42] M. Riquelme, A. Osorio, and E. Quataert. Stochastic electron acceleration by the whistler instability in a growing magnetic field. *The Astrophysical Journal*, 850(2):113, 2017.
- [43] M. A. Riquelme, E. Quataert, P. Sharma, and A. Spitkovsky. Local two-dimensional particle-in-cell simulations of the collisionless magnetorotational instability. *The Astrophysical Journal*, 755(1):50, 2012.
- [44] M. A. Riquelme, E. Quataert, and D. Verscharen. Pic simulations of the effect of velocity space instabilities on electron viscosity and thermal conduction. *The Astrophysical Journal*, 824(2):123, 2016.
- [45] M. E. Rowan, L. Sironi, and R. Narayan. Electron and proton heating in transrelativistic magnetic reconnection. *The Astrophysical Journal*, 850(1):29, 2017.
- [46] M. E. Rowan, L. Sironi, and R. Narayan. Electron and proton heating in transrelativistic guide field reconnection. *arXiv preprint arXiv:1901.05438*, 2019.
- [47] D. Schnitzeler, R. Eatough, K. Ferrière, M. Kramer, K. Lee, A. Noutsos, and R. Shannon. Radio polarimetry of galactic centre pulsars. *Monthly Notices of the Royal Astronomical Society*, 459(3):3005–3011, 2016.
- [48] N. I. Shakura and R. A. Sunyaev. Black holes in binary systems. Observational appearance. *Astronomy and Astrophysics*, 24:337–355, 1973.
- [49] L. Sironi. Electron heating by the ion cyclotron instability in collisionless accretion flows. ii. electron heating efficiency as a function of flow conditions. *The Astrophysical Journal*, 800(2):89, 2015.
- [50] L. Sironi and R. Narayan. Electron heating by the ion cyclotron instability in collisionless accretion flows. i. compression-driven instabilities and the electron heating mechanism. *The Astrophysical Journal*, 800(2):88, 2015.
- [51] L. Sironi and A. Spitkovsky. Acceleration of particles at the termination shock of a relativistic striped wind. *The Astrophysical Journal*, 741(1):39, 2011.
- [52] P. Snyder, G. Hammett, and W. Dorland. Landau fluid models of collisionless magnetohydrodynamics. *Physics of Plasmas*, 4(11):3974–3985, 1997.
- [53] D. J. Southwood and M. G. Kivelson. Mirror instability: 1. physical mechanism of linear instability. *Journal of Geophysical Research: Space Physics*, 98(A6):9181–9187, 1993.
- [54] P. Sweet. The production of high energy particles in solar flares. *Il Nuovo Cimento*

(1955-1965), 8(2):188–196, 1958.

- [55] A. Timokhin and J. Arons. Current flow and pair creation at low altitude in rotation-powered pulsars’ force-free magnetospheres: space charge limited flow. *Monthly Notices of the Royal Astronomical Society*, 429(1):20–54, 2012.
- [56] D. A. Uzdensky. Magnetic reconnection in extreme astrophysical environments. *Space science reviews*, 160(1-4):45–71, 2011.
- [57] J. Villasenor and O. Buneman. Rigorous charge conservation for local electromagnetic field solvers. *Computer Physics Communications*, 69(2-3):306–316, 1992.
- [58] G. R. Werner, D. A. Uzdensky, M. C. Begelman, B. Cerutti, and K. Nalewajko. Non-thermal particle acceleration in collisionless relativistic electron–proton reconnection. *Monthly Notices of the Royal Astronomical Society*, 473(4):4840–4861, 2018.
- [59] F. Xiao, Q. Zhou, H. Zheng, and S. Wang. Whistler instability threshold condition of energetic electrons by kappa distribution in space plasmas. *Journal of Geophysical Research: Space Physics*, 111(A8), 2006.
- [60] K. Yee. Numerical solution of initial boundary value problems involving Maxwell’s equations in isotropic media. *IEEE Transactions on antennas and propagation*, 14(3):302–307, 1966.
- [61] B. Zhang and H. Yan. The internal-collision-induced magnetic reconnection and turbulence (icmart) model of gamma-ray bursts. *The Astrophysical Journal*, 726(2):90, 2010.
- [62] V. Zhdankin, D. A. Uzdensky, G. R. Werner, and M. C. Begelman. Electron and ion energization in relativistic plasma turbulence. *Phys. Rev. Lett.*, 122:055101, Feb 2019.
- [63] E. G. Zweibel and M. Yamada. Magnetic reconnection in astrophysical and laboratory plasmas. *Annual review of astronomy and astrophysics*, 47:291–332, 2009.

# Appendix A

## The Chew-Goldberg-Low Equation of State

In many particle systems, the main physical magnitudes are macroscopic quantities such as temperature, pressure, and density. One way to understand the macroscopic state of the system is via an equation of state that relates two or more of these quantities. Usually, this equation considers equipartition of the energy, because the collisions transfer energy between the particles, thermalizing and isotropizing the system. In magnetized collisionless plasmas the energy transfer between particles is not effective, so the equation of state for an ideal gas is not a good approximation.

In magnetized plasmas, the magnetic field plays a crucial role in the equation of state that describes, at least in a certain regime, the whole system. The presence of an external magnetic field gives the plasma a privileged direction. And considering slow variations in this field, there are adiabatic invariants, which are useful for finding the equation of state.

The adiabatic invariance condition is that, under slow variations of the parameters of a system, in a periodic motion the action integral

$$J = \oint p dq \tag{A.1}$$

is a constant of motion, generally called an adiabatic invariant [25], where  $p$  and  $q$  are the momentum conjugate and the position coordinates. For example, in the case of the harmonic oscillator described by the Lagrangian

$$L = \frac{m}{2} \left( \frac{dx}{dt} \right)^2 - \frac{kx^2}{2} \tag{A.2}$$

and considering  $p = m\dot{x}$ , the momentum can be written in terms of the position and the amplitude of the oscillation

$$p^2 = m^2\omega^2(A^2 - x^2) \tag{A.3}$$

with  $\omega = \sqrt{k/m}$ . The calculus of the action integral in periodic motion is from  $-A$  to  $A$  and then from  $A$  to  $-A$ , due to the symmetry of the system it is equivalent to two times the integral from  $-A$  to  $A$ . Considering the change of variables  $x/A = \sin(\theta)$

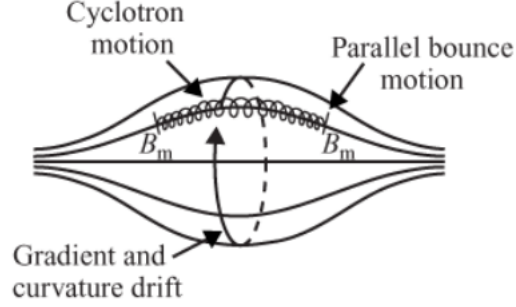


Figure A.1: The three types of motion for a particle trapped in an axially symmetric magnetic mirror field

$$J = 2m\omega \int_{-A}^A \sqrt{A^2 - x^2} dx = 2mA^2\omega \int_{-\pi/2}^{\pi/2} \cos^2(\theta) d\theta = m\pi A^2\omega \quad (\text{A.4})$$

with  $J$  being adiabatic invariant under slow variations of  $\omega$ .

In the presence of a magnetic mirror (like the one described in Fig A.1), the charged particles motion can be separated in the circular orbit around the magnetic field lines, the parallel bounce motion along the magnetic field lines, and the gradient and curvature drift. The last motion depends on the axial symmetry of the magnetic field. Our interest is in the first two motions.

## A.1 The First Adiabatic Invariant

The circular orbit is described by the equations of motion of a charged particle moving in a uniform magnetic field  $B_z$ , which are

$$m \frac{dv_x}{dt} = qv_y B_z \quad \text{and} \quad m \frac{dv_y}{dt} = -qv_x B_z \quad (\text{A.5})$$

These equations can be combined to produce two harmonic oscillator equations with the same frequency  $\omega_c = |q|B_z/m$

$$\frac{d^2x}{dt^2} + \omega_c^2 x = 0' \quad \text{and} \quad \frac{d^2y}{dt^2} + \omega_c^2 y = 0 \quad (\text{A.6})$$

As we previously saw the action integral for the harmonic oscillator:

$$J = \pi m \omega_c \rho_c^2 \quad (\text{A.7})$$

is invariant under slow variations in  $\omega_c$ , where  $\rho_c$  is the Larmor radius. This expression is the same as the magnetic moment, except for a multiplicative constant.

$$\mu = \frac{mv_{\perp}^2}{2B} \quad (\text{A.8})$$

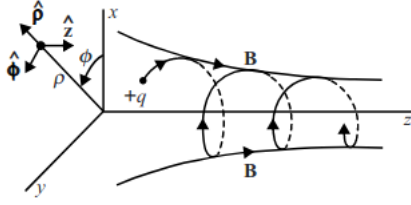


Figure A.2: The coordinate system used for analyzing the motion of a charged particle in a magnetic mirror field.

where  $v_{\perp}$  is the component of the velocity that is perpendicular to the magnetic field.

## A.2 The Second Adiabatic Invariant

The parallel bounce motion is another quasi-periodic motion. This movement is a consequence of the so-called magnetic mirror fields, which is a configuration in which the intensity of the magnetic field varies along the field lines. Consider a magnetic field configuration with axial symmetry, like the one shown in Figure A.1. Writing the Maxwell equation  $\nabla \cdot \mathbf{B} = 0$  in cylindrical coordinates, we have:

$$\frac{1}{\rho} \frac{\partial}{\partial \rho} (\rho B_{\rho}) + \frac{\partial B_z}{\partial z} = 0. \quad (\text{A.9})$$

Assuming that  $\partial B_z / \partial z$  is independent of  $\rho$ , gives

$$B_{\rho} = -\frac{1}{2} \left( \frac{\partial B_z}{\partial z} \right) \rho. \quad (\text{A.10})$$

or in cartesian coordinates

$$B_x = -\frac{1}{2} \left( \frac{\partial B_z}{\partial z} \right) x, \quad \text{and} \quad B_y = -\frac{1}{2} \left( \frac{\partial B_z}{\partial z} \right) y. \quad (\text{A.11})$$

The motion along the  $z$ -axis for a particle with charge  $q > 0$  is given by the Lorentz equation

$$m \frac{dv_z}{dt} = q[v_x B_y - v_y B_x] = -\frac{q}{2} \left( \frac{\partial B_z}{\partial z} \right) (v_x y - v_y x). \quad (\text{A.12})$$

For sufficiently slow magnetic field variations, the motion in the  $x$ - $y$  axes is very close to a circular motion

$$x = \rho_c \sin \omega_c t, \quad \text{and} \quad y = \rho_c \cos \omega_c t. \quad (\text{A.13})$$

While motion along the  $z$ -axis is given by

$$m \frac{dv_z}{dt} = -\frac{\partial B_z}{\partial z} \left( \frac{q}{2} \omega_c \rho_c^2 \right). \quad (\text{A.14})$$

This means that the particles are repelled by the gradient of the magnetic field parallel to their direction of motion, causing the characteristic bouncing of magnetic mirrors. For this motion, the action integral can be written

$$J = m \oint v_{\parallel} d\ell, \quad (\text{A.15})$$

where  $d\ell$  is the path line between the mirrors. The value  $v_{\parallel}$  can be determined by the energy conservation, and the integral can be simplified using the conservation of the magnetic moment.

$$\frac{mv_{\parallel}}{2} + \frac{mv_{\perp}}{2} = \frac{mv_{\parallel}}{2} + \mu B(r) = \mu B_m, \quad (\text{A.16})$$

where  $B(r)$  and  $B_m$  are the magnetic field in the position of the particle, and in the mirrors points, respectively. On the left side of the equation, the energy perpendicular to the magnetic field was written in terms of the magnetic moment, and on the right side, the energy was evaluated at the mirror point.

So  $J$  can be written as

$$J = \sqrt{2\mu m B_m} \oint \sqrt{1 - \frac{B(r)}{B_m}} d\ell. \quad (\text{A.17})$$

### A.3 Equation of state

In order to obtain the equations of state we are going to use the previous results. First, considering a coordinate system at rest with respect to the plasma, the perpendicular pressure is the product of the density and the kinetic energy due to the perpendicular motion

$$P_{s,\perp} = n_s \langle K_{s,\perp} \rangle = n_s \mu_s B \quad (\text{A.18})$$

Considering that  $\mu_s$  is constant the first equation of state for the perpendicular component of pressure is

$$\frac{d}{dt} \left( \frac{P_{s,\perp}}{n_s B} \right) = 0 \quad (\text{A.19})$$

Following the same procedure, the parallel pressure in the reference system of the plasma is

$$P_{s,\parallel} = n_s K_{s,\parallel} \quad (\text{A.20})$$

To write the parallel component of the kinetic energy in terms of the constant and known values, we first consider the equation A.15, and estimate the value of  $J$  as  $v_{\parallel} L$  with  $L$  the distance between the mirror points. Then considering a volume with cross section  $A$ ,

perpendicular to the magnetic field, and length  $L$ . The conservation of mass implies  $n_s AL = \text{constant}$ , and magnetic flux  $BA = \text{constant}$  it closes the system of equations. Putting all together, the parallel component of the kinetic energetic

$$\langle K_{s,\parallel} \rangle \propto \frac{n_s^2}{B^2} \quad (\text{A.21})$$

So the parallel component of the pressure satisfies the equation of state

$$\frac{d}{dt} \left( \frac{P_{s,\parallel} B^2}{n_s^3} \right) = 0 \quad (\text{A.22})$$

The set of equations A.19 and A.22 are the Chew-Goldberg-Low (CGL) equation of State [13], that describes the evolution of the different pressure tensor components in the absence of collisions.

# Appendix B

## Lack of collision between electrons and ions

### Radiative Inefficient Accretion Flow (RIAF)

In order to understand the accretion flow near Sgr A\*, it is important to note that this system is modeled as a Radiative Inefficient Accretion Flow (RIAF). This means that in this system the energy transfer from ions to electrons occurs rather inefficiently. This is because the time required to transfer energy between species is longer than the time in which the particles are accreted. In order to check this condition in Sgr A\*, we will compare the bolometric luminosity  $L \approx 10^{36}$  ergs s<sup>-1</sup> [3, 4] obtained by *Chandra* with the expected luminosity considering the Bondi accretion rate.

To obtain the accretion rate  $\dot{M}$ , we integrate the continuity equation in a sphere of radius  $R$  and considering an isotropic medium we have

$$\dot{M} = 4\pi R^2 \rho v_r, \quad (\text{B.1})$$

where  $\rho$  is the mass density and  $v_r$  is the infall velocity of the plasma.

To fix the parameter  $R$  we consider the Bondi radius, that is the distance from the source where the escape velocity is the sound speed in the medium. This means that only the supersonic particles can escape from the influence of the gravitational potential of the source. Considering a gas composed mainly of protons and electrons, we have:

$$R_B \approx \frac{M_\bullet G m_i}{(5/3) k_B T_i}, \quad (\text{B.2})$$

where  $M_\bullet$  is the mass of Sgr A\*,  $m_i$  and  $T_i$  are the proton mass and temperature,  $k_B$  and  $G$  are the Boltzmann constant and gravitational constant, and the 5/3 factor is the adiabatic index for a monoatomic gas.

Replacing the equation B.2 in B.1, and using  $v_r$  as the sound speed in the gas we can estimate the Bondi radius and the accretion rate. Considering  $M_\bullet \approx 4 \times 10^6 M_\odot$ ,  $k_B T_i \approx 2$  keV and  $n_i \approx 130 \text{ cm}^{-3}$  [4], we get  $\dot{M}_{acc} \approx 7 \times 10^{-5} M_\odot \text{ yr}^{-1}$  and  $R_B \approx 0.05 \text{ pc} \approx 1''$  that is comparable with the resolution of *Chandra*. If gas were accreting at this rate into the BH via a thin accretion disk [48], using the model that successfully reproduce the luminosity of accreting sources (e.g., [29]), the luminosity would be  $L \approx 0.1 \dot{M}_B c^2 \approx 4 \times 10^{41} \text{ ergs s}^{-1}$ , This is five orders of magnitude larger than the observed bolometric magnitude. This analysis thus favor the models in which very little energy of the gravitational potential of the inflowing gas is radiated.

The main particles that radiate are the electrons, so the fact that the observed radiation is lower than the predicted radiation has two possible explanations. First, electrons and ions have different temperatures. If the electrons are colder than the ions, the radiation must be lower than the case of both species at the same temperature. The second possibility is that there are large outflows of particles that decrease the luminosity. The ratio between electron temperature and ion temperature required to explain the low radiative efficiency is unknown and depends on the properties of the outflow, which are also unknown. Contributing to finding out the expected ratio between the electron and ion temperatures in systems like Sgr A\* is the main goal of this thesis. Solving this problem involves nontrivial kinetic plasma physics, mainly because of the expected lack of Coulomb collisions between species as we explain below.

## Thermalization time

The lack of collisions between ions and electrons can be inferred by comparing the time required for the plasma to exchange energy between species ( $\tau_{ep}$ ) with the time required for the plasma to be accreted into the black hole ( $\tau_{acc}$ ) from the Bondi radius. From [35] we have:

$$\tau_{ep} = \frac{\sqrt{2\pi}}{2n_e \sigma_T c \ln \Lambda} \frac{m_p}{m_e} (\theta_e + \theta_p)^{3/2} \simeq 9.3 \times 10^{-5} \alpha \theta_e^{3/2} \tilde{m} \dot{m}^{-1} r^{3/2} \text{ s}, \quad (\text{B.3})$$

$$\tau_{acc} = \int \frac{dR}{v(R)} \simeq 1.8 \times 10^{-5} \alpha^{-1} \tilde{m} r^{3/2} \text{ s}. \quad (\text{B.4})$$

where  $n_e$  is the electrons number density,  $\sigma_T$  is the Thomson cross section,  $\ln \Lambda \approx 20$  is the Coulomb logarithm,  $m_e$  and  $m_p$  are the mass of the electrons and protons respectively,  $\theta_e = k_B T_e / m_e c^2$  and  $\theta_p = k_B T_p / m_p c^2$  are the dimensionless electron and proton temperature,  $\alpha$  is a measure of the viscosity (a typical value for these type of objects is  $\alpha = 0.3$ ),  $\tilde{m} = M / M_\odot$  is the mass of the central object in solar mass units ( $M_\odot \approx 2 \times 10^{30}$  kg),  $\dot{m}$  is the accretion rate in Eddington units ( $\dot{m} = \dot{M} / \dot{M}_{\text{edd}}$ , where  $\dot{M}$  is the accretion rate, and  $\dot{M}_{\text{edd}} = 1.39 \times 10^{18} \tilde{m} \text{ g s}^{-1}$ ), and  $r = R / R_s$  is the distance from the central object in Schwarzschild units ( $R_s = 2.95 \tilde{m} \text{ km}$ ).

Dividing equations B.3 with B.4 we get:  $\tau_{ep} / \tau_{acc} \approx 5 \alpha^2 \theta_e^{3/2} \tilde{m}^{-1}$ . With this equation, we can estimate the radius at which the time between collisions is equal to the accretion time. Assuming that the value of  $\alpha$  and  $\dot{m}$  remain constant, at  $\alpha \sim 0.3$  and  $\dot{m} \sim 10^{-3}$ , and  $\theta_e$

increases by potential energy transfer as

$$\theta_e(r) = \theta_e(R_B) - \frac{2GM_\bullet}{3R_Bc^2} \left(1 - \frac{R_B}{r}\right) \sim 4 \times 10^{-3} - 2 \times 10^{-6} \left(1 - \frac{0.05 \text{ pc}}{r}\right), \quad (\text{B.5})$$

imposing  $\tau_{ep}/\tau_{acc} = 1$  we can estimate the radius at which collisions are no longer important

$$\theta_e(r) \approx \left(\frac{\dot{m}}{5\alpha^2}\right)^{2/3} \sim 10^{-2}, \quad (\text{B.6})$$

$$r_c \sim 10^{-5} \text{ pc} \sim 3 \times 10^8 \text{ km} \sim 25R_s. \quad (\text{B.7})$$

For radius smaller than  $r_c$  the plasma can be considered non-collisional, this means that the different species that compound the plasma can have different temperatures, and electrons are expected to be colder than the ions (see e.g. [37]).

# Appendix C

## Magnetic Amplification

In the vicinity of Sgr A\*, due to differential rotation around the black hole and disk turbulence, the plasma fluid velocity is expected to acquire a shear-like profile. In the ideal magnetohydrodynamics prescription<sup>1</sup>, the magnetic field evolves without the term of resistivity as follows:

$$\frac{\partial \vec{B}}{\partial t} = \nabla \times (\vec{U} \times \vec{B}). \quad (\text{C.1})$$

Considering the shear-like velocity profile:

$$\vec{U} = -sy\hat{x}, \quad (\text{C.2})$$

where  $s$  is the shear rate, and  $y$  is the coordinate in the  $\hat{y}$  direction.

Replacing C.2 in C.1 we found that the magnetic field increases or decreases depending on its initial direction.

$$\frac{\partial \vec{B}}{\partial t} = -sB_y\hat{x}. \quad (\text{C.3})$$

Where  $B_y$  is the  $y$  component of the magnetic field.

This effect depends on the presence of an initial magnetic field. Some measurements constrain the magnetic field near Sgr A\* in our line-of-sight to  $B \sim 16 - 33 \mu\text{G}$ , at a distance of  $\lesssim 150pc$  from the black hole [47]<sup>2</sup>. In this thesis, we study the case when the magnetic field grows.

---

<sup>1</sup>The ideal magnetohydrodynamic is a good prescription when magnetic Reynold number is large  $R_m (\equiv \mu_0\sigma UL \gg 1$ , with  $\mu_0$  the permeability of free space,  $\sigma$  the conductivity of the plasma,  $U$  is the characteristic velocity and  $L$  is the length-scale that characterized the spatial gradients in the fluid)

<sup>2</sup>The magnetic field along the line of sight was estimated measuring the Faraday rotation of pulsars that are near the Galactic center

In a growing magnetic field, as a consequence of the lack of collisions, and the conservations of the magnetic moment and of the second adiabatic invariant (see Appendix A), the plasma presents pressure anisotropy, where the perpendicular pressure ( $P_{\perp}$ ) to the direction of the mean magnetic field increases, while the component of the pressure that is parallel ( $P_{\parallel}$ ) to the magnetic field decreases ( $P_{\perp} > P_{\parallel}$ ). In the first stages of the amplification of the magnetic field the pressure evolves following the C.G.L equations of state (see also AppendixA), generating the pressure anisotropy. This anisotropy produces electromagnetics instabilities in the plasma such as whistler, mirror, and Ion-Cyclotron (IC). When the instabilities reach some threshold in their amplitude, the anisotropy starts to be damped by scattering and reaches a marginal equilibrium, breaking the conservations of the invariants.

# Appendix D

## Viscous heating

The macroscopic state of the plasma is described by the distribution function of each species ( $f_s$ ), which quantifies the particle density of the species  $s$  in the six-dimensional phase space ( $f_s \equiv \frac{N_s}{(\Delta x)^3(\Delta v)^3}$ ). Its evolution is described by the Vlasov equation

$$\frac{\partial f_s}{\partial t} + \vec{v} \cdot \nabla f_s + \frac{q_s}{m_s} (\vec{E} + \vec{v} \times \vec{B}) \cdot \nabla_{\vec{v}} f_s = \left( \frac{\delta f_s}{\delta t} \right)_c \quad (\text{D.1})$$

where  $\nabla_{\vec{v}}$  is the gradient in the velocity space, and  $\left( \frac{\delta f_s}{\delta t} \right)_c$  is the change of the distribution function via collisions with other species.

From Eq. D.1 we can obtain the moment equations, which are the result of multiplying the Vlasov equation by powers of the velocity and integrating over the velocity space. Our interest is in the second order moment equation (the result of multiplying D.1 by  $m_s v^2/2$  and integrating over  $\vec{v}$ ), which gives the evolution of the mean kinetic energy of the plasma in an arbitrary reference system. Expressing our result in the reference system of the fluid (replacing  $\vec{v} \rightarrow \vec{u} + \vec{U}_s$ , where is  $\vec{U}_s$  the mean velocity of the species  $s$ ) we get:

$$\frac{d}{dt} \left( \frac{3}{2} p_s \right) = -\nabla \cdot \vec{q}_s - \frac{5}{2} p_s \nabla \cdot \vec{U}_s - \overleftrightarrow{\sigma}_s : \nabla \vec{U}_s + W_s, \quad (\text{D.2})$$

where  $:$  is a double dot product,  $p_s \equiv Tr(\overleftrightarrow{P}_s/3)$  is the trace of the pressure (which is simply the pressure in the isotropic case). This way the pressure tensor is defined as  $\overleftrightarrow{P}_s = \overleftrightarrow{\sigma}_s + \mathbb{1} p_s$ , where  $\overleftrightarrow{\sigma}_s$  is its traceless component.  $W_s$  and  $\vec{q}_s$  are the heating rate of the species “ $s$ ” due to collisions with other species and the heat flux, respectively.

From equation D.2 we see that depending on the plasma velocity profile, the traceless component of the pressure tensor can give rise to heating by an effective viscosity.

If the plasma velocity profile is non-compressive (as in Equation C.2), the second term on the right-hand side of D.2 is zero, and the third term becomes (see e.g. [30, 52]):

$$\overleftrightarrow{\sigma}_s : \nabla \vec{U}_s = \sigma_{sxy} \frac{\partial U_{sx}}{\partial y} = -s \hat{b}_x \hat{b}_y (P_\perp - P_\parallel), \quad (\text{D.3})$$

where  $\hat{b}_x$  and  $\hat{b}_y$  are the  $x$  and  $y$  component of the magnetic field normalized by the magnitude of the mean magnetic field, respectively. The term  $-s \hat{b}_x \hat{b}_y$  corresponds to the growth rate of the magnetic field ( $(dB/dt)/B \equiv q$ ). Depending on the anisotropy and the fields this can represent a cooling or heating. In our case, this term corresponds to heating, because the perpendicular pressure is larger than the parallel, and from C.3 we see that the product  $\hat{b}_x \hat{b}_y$  is negative.

In summary, in a homogeneous and isotropic plasma under a uniform magnetic field that grows in time, the anisotropy ( $\Delta P \equiv P_\perp - P_\parallel$ ) grows as a consequence of the conservation of the adiabatic invariances,  $\frac{d(P_\perp/B)}{dt} = 0$  and  $\frac{d(P_\parallel B^2)}{dt} = 0$ . This anisotropy is regulated by fluctuations in the magnetic field that scatter particles. The heating shown in D.3 is regulated by the presence of the instabilities that also appear by the anisotropy.

The viscous heating is a heating way where the particles gain energy due to their own anisotropy, even in the absence of direct interaction between the particles.

# Appendix E

## Second-order Fermi acceleration

Second-order Fermi acceleration was proposed by Fermi [17]. In this process, charged particles move between magnetic field clouds and collide repeatedly with magnetic field fluctuations, on average, gaining energy.

Let us consider a magnetic cloud moving to the right with speed  $U_o$ , and a charged particle with momentum  $\vec{p}_0$  and moving to the left with an angle of inclination  $\theta$  with respect to  $\vec{U}_o$ , as shown in the Fig. E.1.

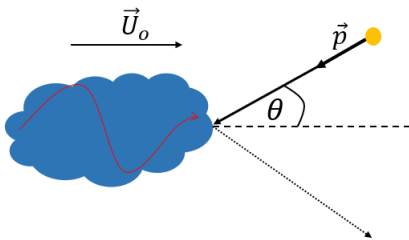


Figure E.1: Schematic picture of the collision between a charged particle and a magnetic cloud.

The energy and momentum of the particle on the  $x$ -axis are related as follows:

$$p_{0,x} = -p_0 \cos(\theta) = -\sqrt{\frac{E^2}{c^2} - m^2 c^2} \cos(\theta), \quad (\text{E.1})$$

where  $m$  and  $c$  are the particle mass and the speed of light.

If we move to the reference frame that goes with the magnetic cloud, the energy and momentum of the particle are modified as follows

$$E' = \gamma_o(E + U_o p_0 \cos(\theta)) \quad \text{and} \quad p'_x = \gamma_o(p_{0,x} - \frac{EU_o}{c^2}), \quad (\text{E.2})$$

where  $\gamma_o$  is the Lorentz factor of the cloud. The other two components of the momentum remain unchanged.

In this reference frame, the collision of the particle with the cloud only changes the sense of the momentum in the  $x$ -axis, preserving the other two components and the energy.

$$p_{f,x} = -\gamma_o(p_{0,x} - \frac{EU_o}{c^2}) \quad (\text{E.3})$$

In the laboratory reference system, the particle energy is:

$$E'' = \gamma_o(E' + U_o p_{f,x}) = \gamma_o^2(E(1 + \frac{U_o^2}{c^2}) + 2U_o p_0 \cos(\theta)). \quad (\text{E.4})$$

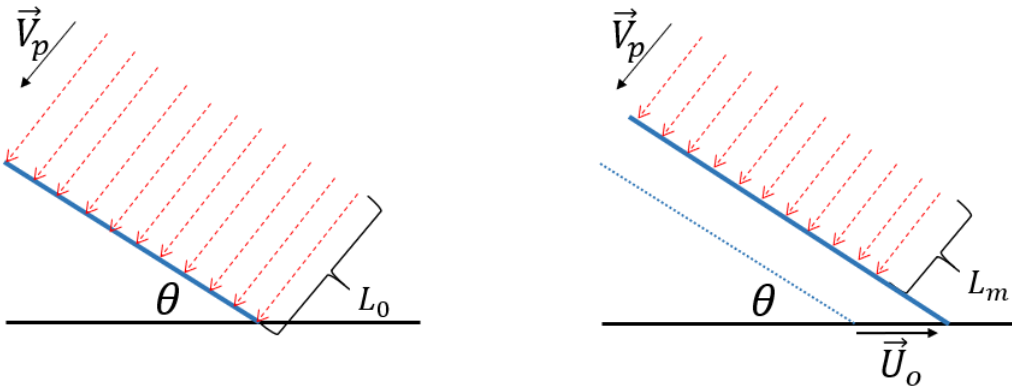
The normalized energy difference for the initial kinetic energy ( $E - mc^2$ ) is

$$\frac{\Delta E}{E_{kin}} = \frac{2U_o \gamma_o^2 \gamma_p}{c^2(\gamma_p - 1)}(U_o + V_p \cos(\theta)), \quad (\text{E.5})$$

where  $V_p$  and  $\gamma_p$  are the speed and the Lorentz factor of the particle, respectively.

At this point we know how much energy a particle gains after a collision. In order to know the mean energy gain, we must take the average, taking into account the probability of each collision.

The probability of collision is inversely proportional to the time between collisions of the particles with the magnetic cloud. Consider a cloud is an inclined plane with an inclination angle  $\theta$  that originally does not move, as shown in Fig. 1a. Here the particles are at a distance  $L_0$  take a time  $T_0(\equiv L_0/V_p)$  to cross the plane. In this situation, all particles have an equal probability of reaching the plane. If the plane moves in the direction  $x$  with speed  $U_o$ , as shown in Fig. 1b, the distance  $L_m$  the particles must travel to reach the plane is:



(a) Scheme of the distance traversed by the particles when the magnetic cloud is at rest. (b) Scheme of the distance traversed by particles when the magnetic cloud is in motion

$$L_m = L_0 - U_o \cos(\theta)T_m, \quad (\text{E.6})$$

where  $T_m$  is the time it takes for particles to reach the plane, which is given by:

$$T_m = \frac{L_m}{V_p} = \frac{L_0}{V_p} - \frac{U_0}{U_p} \cos(\theta) T_m \quad \Rightarrow \quad T_m = \frac{T_0}{1 + \frac{U_0}{V_p} \cos(\theta)}. \quad (\text{E.7})$$

So the probability of the particles colliding with the magnetic cloud depends on the angle of incidence,  $P(\theta) = A(1 + \frac{U_o}{V_p} \cos(\theta))$ , with  $A$  a normalization constant.

$$\int P(\theta) d\Omega = A \int_0^{2\pi} d\phi \int_0^\pi \sin(\theta) d\theta (1 + \frac{U_o}{V_p} \cos(\theta)) \quad \Rightarrow \quad P(\theta) = \frac{1}{4\pi} (1 + \frac{U_o}{V_p} \cos(\theta)). \quad (\text{E.8})$$

With this, we can obtain the average energy gain.

$$\begin{aligned} \langle \frac{\Delta E}{E_{kin}} \rangle &= \int P(\theta) \frac{\Delta E}{E_{kin}} d\Omega = \frac{8}{3} \gamma_o^2 \frac{U_o^2}{c^2} \left( \frac{\gamma_p}{\gamma_p - 1} \right) \\ &= \frac{8}{3} \gamma_o^2 \frac{U_o^2}{V_p^2} \left( \frac{\gamma_p + 1}{\gamma_p} \right). \end{aligned} \quad (\text{E.9})$$

This is the average energy gain at each scattering in the plasma. This mechanism is called second order, because it is quadratic in  $U_o/V_p$ , and when the plasma is ultra-relativistic it tends to  $\langle \Delta E/E_{kin} \rangle = (8/3)(U_o/c)^2$ .

# Appendix F

## Magnetic Reconnection

The magnetic reconnection process transfers the energy stored in the magnetic field to the particles by reorganizing the magnetic field lines. This process is usually described in the magnetohydrodynamic regime (MHD). In this regime, reconnection occurs when the frozen flow theorem is broken on time scales smaller than magnetic diffusion [63].

An example of the magnetic field configuration that can support reconnection is the so-called Harris Current Sheet, shown in Fig. F.1, and is given by:

$$\vec{B} = B_0 \tanh\left(\frac{y}{d}\right) \hat{x}, \quad B_0 > 0. \quad (\text{F.1})$$

At the surface  $y = 0$ ,  $B_x = 0$ . For  $y > 0$  the magnetic field points in the direction  $+x$ , while for  $y < 0$ , it points in the direction  $-x$ . The neutral surface  $y = 0$ , represented by a dashed line in Fig. F.1, separates two geometric regions of magnetic field with opposite direction.

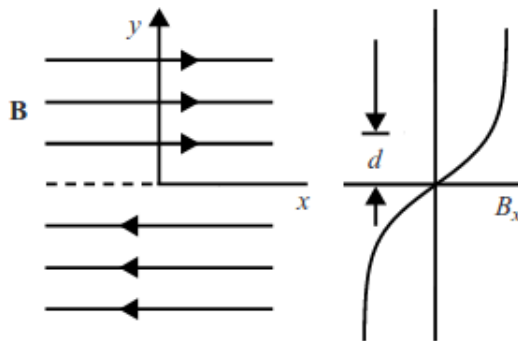


Figure F.1: The magnetic field geometry across planar current sheet. Figure taken from [26]

## F.1 The Sweet–Parker model

The Sweet-parker model [39, 54] is a simple model, which helps to understand how the magnetic reconnection transfers energy to the particles in a configuration like the one given in Eq. F.1, in which the component  $B_x$  tends to  $\pm B_0 \hat{x}$  as  $y \rightarrow \pm\infty$ , and these magnetic fields are convected, towards each other.

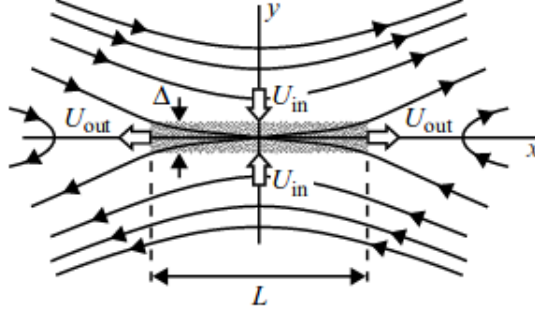


Figure F.2: The magnetic field geometry near reconnection region. Figure taken from [26]

Considering the geometry of Fig F.2, and imposing that the system is in steady state, the equation of momentum balance along the  $y$  axis, considering uniform density, gives:

$$P_{cs} = \frac{1}{2}\rho_m U_{in}^2 + \frac{B_0^2}{8\pi}, \quad (\text{F.2})$$

where  $P_{cs}$  is the pressure in the current sheet region ( $-\Delta/2 < x < \Delta/2$ , and  $-L/2 < y < L/2$ ).

By performing the same procedure along of the current sheet, the plasma output velocity can be obtained in the regions  $x = \pm L/2$ .

$$\frac{1}{2}\rho_m U_{out}^2 = P_{cs} = \frac{1}{2}\rho_m U_{in}^2 + \frac{B_0^2}{8\pi}. \quad (\text{F.3})$$

This result gives us an idea of the transfer of energy from the magnetic field to the motion of the plasma. Magnetic reconnection is a subject of active research in different scenarios such as solar flares[15],  $\gamma$ -ray bursts [61] and accretion flows around supermassive black holes [56].

# Appendix G

## The Code

A plasma is a collection of charged particles, which typically is globally neutral. The motion of each particle is described by the Lorentz force. At the same time, the electric current produced by each particle affects the evolution of the electric and magnetic fields, which are described by Maxwell's equations.

A plasma is composed of a large number of particles, so its evolution can be prescribed via the Boltzmann equation:

$$\frac{\partial f_s}{\partial t} + \frac{\vec{p}}{m\gamma} \cdot \nabla f_s + q_s(\vec{E} + \frac{\vec{v}}{c} \times \vec{B}) \cdot \nabla_{\vec{p}} f_s = \left( \frac{\delta f_s}{\delta t} \right)_c, \quad (\text{G.1})$$

which, when complemented with Faraday's and Ampere's laws:

$$\nabla \times \vec{E} = -\frac{1}{c} \frac{\partial \vec{B}}{\partial t}, \quad (\text{G.2})$$

$$\nabla \times \vec{B} = \frac{4\pi}{c} \vec{J} + \frac{1}{c} \frac{\partial \vec{E}}{\partial t}, \quad (\text{G.3})$$

describes the whole evolution of the plasma. The term at the right hand side of Eq. G.1 accounts for the binary collisions between particles. In the collisionless regime, of interest to this thesis, this term is neglected and Eq. G.1 becomes the Vlasov equation. Thus, the Vlasov equation, complemented with Faraday's and Ampere's equations (the "Vlasov-Maxwell system"), gives the evolution of the distribution function of each species, as well as the evolution of the electromagnetic fields. The current  $\vec{J}$  in Equation G.3 can be computed with the distributions function( $f_s$ ) of the species.

$$\vec{J}(\vec{r}, t) = \sum_s \frac{q_s}{m_s} \int \vec{p} f_s(\vec{r}, \vec{p}, t) d^3 p \quad (\text{G.4})$$

This set of equations model a collisionless plasma from first principles.

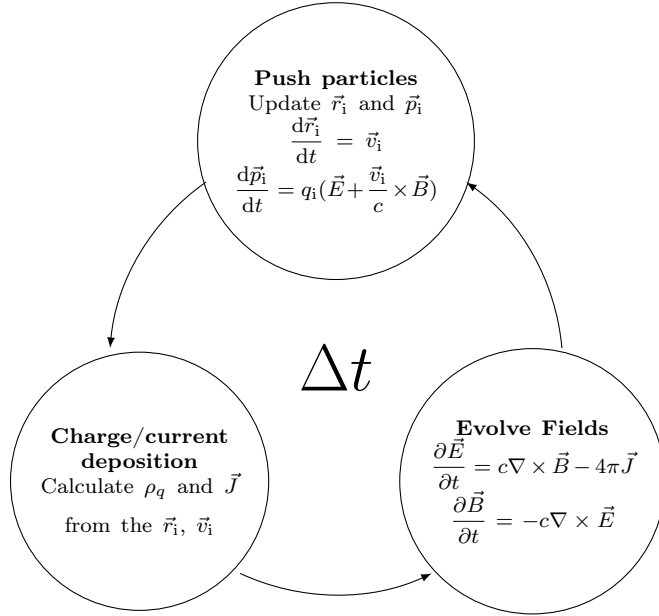


Figure G.1: The PIC cycle during a time step  $\Delta t$ .

In solving the Vlasov-Maxwell system numerically, two approaches are usually used. The first one is to consider the distribution function evolving in six-dimensional continuous phase space, and solving with some Eulerian or Lagrangian method [12, 16]. This method has the advantage of being free of noise but has a large numerical cost related to the multidimensional problems (6D) and the cutoff of the distributions functions. The other approach is the particle-in-cell (PIC) method where the motion of the particles is solved for each particle.

The PIC method is equivalent to solve the Vlasov equation, this can be check considering the point-like particle distribution function

$$f(\vec{r}, \vec{p}, t) \approx \sum_k w_k \delta(\vec{r} - \vec{r}_k) \delta(\vec{p} - \vec{p}_k) \quad (\text{G.5})$$

Where  $\delta$  are the delta Dirac function and  $w_k$  is the particle weight. The number of particles has to be very high for a good sampling of the phase space distribution. However, this number is always much smaller than the number of particles in real plasmas.

In a plasma, in principle, each particle feels the electromagnetic field produced by all the other particles. Summing over all binary interactions the number of computations grows as  $N(N-1)/2 \approx N^2$ . To avoid this large computational cost, in PIC simulation the particles do not feel each other directly but via the electromagnetic field in the grid points which results in the evolution of the density and current of the plasma in each grid. Thus the number of operations grows as  $N$  instead  $N^2$ .

## G.1 The algorithm of a PIC code

The basic stages to evolve a PIC code in a time step  $\Delta t$  are shown in Figure G.1:

- I) Update the velocity and position of each particle solving Newton's equations.
- II) Collect the charge and current density of all the particles and deposit them in the grids.
- III) Evolve the electric and magnetic field by solving Maxwell's equations.

We will briefly describe the steps followed by the code:

### G.1.1 Step 1: Pushing particles

The set of equations to be solved are:

$$\frac{d\vec{u}_s}{dt} = \frac{q_s}{m_s c} (\vec{E} + \frac{\vec{u}_s}{\gamma_s} \times \vec{B}), \text{ and} \quad (\text{G.6})$$

$$\frac{d\vec{r}_s}{dt} = \frac{\vec{u}_s c}{\gamma_s}, \quad (\text{G.7})$$

where  $\vec{u}_s = \gamma_s \vec{v}_s / c$  is the 4-velocity of the particle  $s$  divided by the speed of light, and  $\gamma_s = 1/\sqrt{1 - (v_s/c)^2}$  is the Lorentz factor. In order to solve Newton's equations, one of the most used algorithms is the Boris push [7]. This algorithm is based on the leapfrog method. The Boris push is stable, second-order accurate, and conserves energy well. The algorithm defines the particles positions and 4-velocities with half timestep out of phase, with the forces being defined at the same time of positions. The discretized Newton's equations are:

$$\frac{\vec{u}^{n+1/2} - \vec{u}^{n-1/2}}{\Delta t} = \frac{q_s}{m_s c} (\vec{E}^n + \frac{\vec{u}^n}{\gamma^n} \times \vec{B}^n) \text{ and} \quad (\text{G.8})$$

$$\frac{\vec{r}^{n+1} - \vec{r}^n}{\Delta t} = \frac{\vec{u}^{n+1/2} c}{\gamma^{n+1/2}}. \quad (\text{G.9})$$

Rewriting  $\vec{u}^n = (\vec{u}^{n+1/2} + \vec{u}^{n-1/2})/2$  for the right hand side of the equation G.8, the 4-velocity can be solved for  $\vec{u}^{n+1/2}$  when  $\vec{E}^n$  and  $\vec{B}^n$  are known. The last step is to update the particle positions. From the Eq. G.9 it is straightforward to show that

$$\vec{r}^{n+1} = \vec{r}^n + \frac{\vec{u}^{n+1/2} c}{\gamma^{n+1/2}} \Delta t. \quad (\text{G.10})$$

### G.1.2 Step 2: Current deposition

In order to solve Maxwell's equations, we need to know the values of the current density given by the particles. In order to smooth the current density we defined these values on

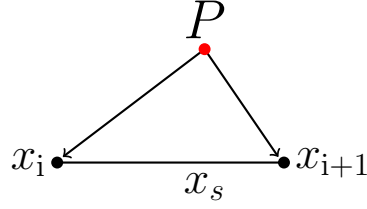


Figure G.2: A weighting technique to interpolate charges and current, where for a particle in a location  $P$  the contribution to the grid point  $x_i$  is given by  $(x_{i+1} - x_s)/(x_{i+1} - x_i)$ , and the contribution to  $x_{i+1}$  is  $(x_s - x_i)/(x_{i+1} - x_i)$

the grid, so each particle deposits their contribution to the nearest grid points. The charge density and current defined in the grid point  $\vec{r}_k$  are written as:

$$\vec{J}(\vec{r}_k) = \sum_s q_s w_s \vec{v}_s S(\vec{r}_k - \vec{r}_s), \quad (\text{G.11})$$

where  $S$  is a shape function that depends on the selected scheme.

One way to put the current is the nearest method, where the particles deposit their current on the nearest grid, this is the fastest way to deposit the current but with a lot of noise. Another method is the linear interpolation between the nearest grids, where the particles deposit their current in all grids associated to their location. This corresponds to the two, four and twelve edges for simulations in one, two and three dimensions, respectively. In one dimension, the current deposition are represented in Figure G.2, and the contribution from the particles contained between  $x_i$  and  $x_{i+1}$  on the grid are:

$$\vec{J}_i = \sum_{s=1}^{N_{ppc}} q_s w_s \vec{v}_s \left(1 - \frac{x_s - x_i}{\Delta x}\right) \quad \text{and} \quad \vec{J}_{i+1} = \sum_{s=1}^{N_{ppc}} q_s w_s \vec{v}_s \left(\frac{x_s - x_i}{\Delta x}\right). \quad (\text{G.12})$$

### G.1.3 Step 3: Evolution of the fields

The evolutions of the electric and magnetic fields are determined by Faraday's and Ampere's laws:

$$\frac{\partial \vec{E}}{\partial t} = c \nabla \times \vec{B} - 4\pi \vec{J} \quad \text{and} \quad (\text{G.13})$$

$$\frac{\partial \vec{B}}{\partial t} = -c \nabla \times \vec{E}. \quad (\text{G.14})$$

Since these equations evolve as a consequence of the current density, the other two Maxwell's equations should be immediately satisfied. However, due to numerical errors, this is not necessarily true. For instance, the current deposition may not conserve charge, in the sense that the continuity equation may not completely describe the evolution of the charge density  $\rho_q$  ( $\partial \rho_q / \partial t + \nabla \cdot \vec{J} \neq 0$ ). In order to solve this problem, there are some methods to improve the

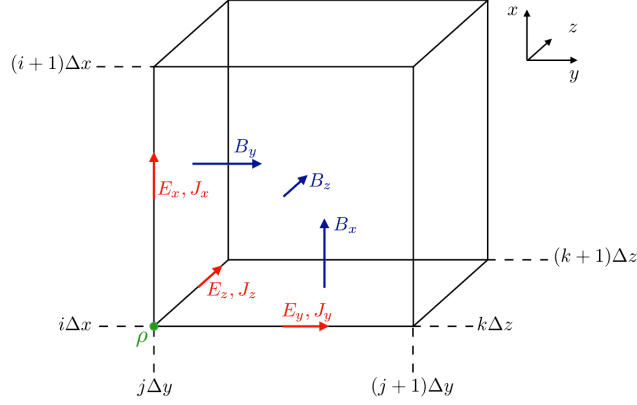


Figure G.3: Spatial distribution of the fields discretized proposed by Yee. The components of the magnetic field  $\vec{B}$  are defined in the faces of the cell and the electric field  $\vec{E}$  are defined in the edges. Figure taken from <http://www.maisondelasimulation.fr/smilei/algorithms.html>

numerical precision [57], which includes solving the Poisson equation to correct the electric field by forcing  $\nabla \cdot \vec{E} = 4\pi\rho_q$ .

In order to solve the evolution of the discretized electromagnetic fields, Maxwell's equations are solved by the Finite-Difference Time-Domain Method (FDTD) proposed by Yee [60]. This method is efficient, stable, and second-order accurate. Here the electric and magnetic fields are decentered in time and space. Figure G.3 shows the spatial decomposition. The spatial domain is divided into cubes, with the magnetic fields defined in the faces of the cubes at the same time as velocities, i.e., at half-integer time steps ( $t_{n+1/2}$ ). The electric fields, on the other hand, are defined in the edges of the cubes and at the same time as the particles locations ( $t_n$ ). This scheme follows the leapfrog algorithm as the Boris push. For example, the  $z$  component of the electric field evolve as follows:

$$\begin{aligned} \frac{(E_z)_{i,j,k+1/2}^{n+1} - (E_z)_{i,j,k+1/2}^n}{\Delta t} = & c \frac{(B_y)_{i+1/2,j,k+1/2}^{n+1/2} - (B_y)_{i-1/2,j,k+1/2}^{n+1/2}}{\Delta x} \\ & - c \frac{(B_x)_{i,j+1/2,k+1/2}^{n+1/2} - (B_x)_{i,j-1/2,k+1/2}^{n+1/2}}{\Delta y}, -4\pi(J_z)_{i,j,k+1/2}^{n+1/2} \end{aligned} \quad (\text{G.15})$$

where  $\Delta t$  is the time step, and  $\Delta x$  and  $\Delta y$  are the spatial step along  $x$  and  $y$ , respectively. This method is stable under the Courant-Friedrichs-Lewy condition:

$$\left(c \frac{\Delta t}{\Delta x}\right)^2 < 1 \quad (1\text{D}) \quad (\text{G.16})$$

$$(c\Delta t)^2 \left(\frac{1}{\Delta x^2} + \frac{1}{\Delta y^2}\right) < 1 \quad (2\text{D}) \quad (\text{G.17})$$

$$(c\Delta t)^2 \left(\frac{1}{\Delta x^2} + \frac{1}{\Delta y^2} + \frac{1}{\Delta z^2}\right) < 1 \quad (3\text{D}) \quad (\text{G.18})$$

## G.2 Boundary conditions

There are some boundary conditions that could be simulated in PIC codes for different purposes. Below we describe briefly some of the boundary conditions that are usually used in PIC codes.

### G.2.1 Particles

- The periodic boundary condition is robust easy to implement and useful in various contexts. This is the case in this thesis, with every time a particle crosses the boundary of the simulation domain, it appears on the other side with the same momentum and energy.
- In the context of absorbing particles or open boundary conditions, the particles that arrive at the borders of the simulation are removed.
- Also, new particles can be injected in the simulations, as the case of pulsar where the rate of pair creation is relevant [11, 55], or in shocks where particles are injected from one side of the simulation in an expanding box with an injector moving backward at speed of light to reduce numerical noise [51].

### G.2.2 Fields

- In the periodic boundary condition, the fields at the end of the spatial domain of simulation are matched with the fields at the beginning of the space. In this case, a spatial domain greater than the longest wavelength triggered in the simulation is needed, to avoid the formation of non-physical modes.
- Absorption of the electromagnetic fields is usually used to simulate open boundary. This is accomplished by adding resistive components to the Maxwell equations in the borders of the simulations, and gradually increasing these resistive terms to avoid undesirable reflections and to make sure that the waves are completely absorbed.

# Appendix H

## One Dimensional simulations

The results of this thesis were obtained using 1D simulations. It is interesting to know the procedure and necessary assumptions that describe plasma evolution in one dimension. For this, we will start from the equations for 2D shear coordinates described in the Appendix of [43], which are in the  $S'$  frame of reference, and we will call  $S''$  to the frame of reference used in the 1D simulations. These two reference systems are related by the following change of coordinate.

$$\begin{aligned}x'' &= x' - \frac{y' st'}{1 + s^2 t'^2}, & y'' &= y', \\z'' &= z', & t'' &= t'.\end{aligned}\tag{H.1}$$

The transformations that relate the shear coordinates  $S'$  with the usual cartesian coordinates  $S$  are:

$$\begin{aligned}x' &= x, & y' &= \Gamma(y - vt), \\z' &= z, & t' &= \Gamma(t - vy/c^2),\end{aligned}\tag{H.2}$$

where  $\Gamma = (1 - \frac{v^2}{c^2})^{-1/2}$ , and  $v = -c \operatorname{arctanh}(sx/c)$  is the shear velocity profile. The simulations in this thesis are in the non-relativistic regime where  $v \approx -sx$ .

To justify the 1D simulations, our study focused on the modes that have a wave vector parallel to the mean magnetic field ( $\vec{k} \parallel \langle \vec{B} \rangle$ ). From the frozen flux theorem, in the  $S''$  frame of reference, the mean magnetic field is always parallel to  $x''$ .

The change of coordinates affects the equations that govern the evolution of the plasma. Therefore, we are going to write the spatial derivatives in  $S'$  using the coordinates  $S''$ .

$$\begin{aligned}
\frac{\partial}{\partial x'} &= \frac{\partial}{\partial x''}, \\
\frac{\partial}{\partial y'} &= \frac{-st'}{1+s^2t'^2} \frac{\partial}{\partial x''} + \frac{\partial}{\partial y''}, \\
\frac{\partial}{\partial z'} &= \frac{\partial}{\partial z''}, \\
\frac{\partial}{\partial t'} &= \frac{\partial}{\partial t''} - y's \frac{1-s^2t'^2}{(1+s^2t'^2)^2} \frac{\partial}{\partial x''}.
\end{aligned} \tag{H.3}$$

In the one-dimensional limit, we consider that the derivatives with respect to  $y''$  and  $z''$  are null ( $\frac{\partial}{\partial y''} = \frac{\partial}{\partial z''} = 0$ ), and the  $y''$  coordinate is negligible when  $0 < y'' < \delta$  with  $\delta \rightarrow 0$ .

## H.1 Evolution of $\vec{E}$ and $\vec{B}$

Considering the evolution of  $\vec{E}'$  and  $\vec{B}'$  in terms of the current  $\vec{J}'$  in the sheared coordinates described in [43], it can be shown that by replacing  $x'$  with our coordinate  $x''$  and keeping only the dimension  $x''$  ( $\frac{\partial}{\partial y''} = \frac{\partial}{\partial z''} = 0$ , and  $0 < y'' < \delta$  with  $\delta \rightarrow 0$ ), the evolution of the fields is given by:

$$\begin{aligned}
\frac{\partial B'_x}{\partial t''} &= c \frac{st''}{1+s^2t''^2} \frac{\partial E'_z}{\partial x''}, \\
\frac{\partial B'_y}{\partial t''} &= c \frac{st''}{1+s^2t''^2} \frac{\partial E'_z}{\partial x''} - sB'_x, \\
\frac{\partial B'_z}{\partial t''} &= \frac{-c}{1+s^2t''^2} \left( \frac{\partial E'_y}{\partial x''} + st'' \frac{\partial E'_x}{\partial x''} \right),
\end{aligned} \tag{H.4}$$

and

$$\begin{aligned}
\frac{\partial E'_x}{\partial t''} &= -c \frac{st''}{1+s^2t''^2} \frac{\partial B'_z}{\partial x''} - 4\pi J'_x, \\
\frac{\partial E'_y}{\partial t''} &= -c \frac{st''}{1+s^2t''^2} \frac{\partial B'_z}{\partial x''} - sE'_x - 4\pi J'_y, \\
\frac{\partial E'_z}{\partial t''} &= \frac{c}{1+s^2t''^2} \left( \frac{\partial B'_y}{\partial x''} + st'' \frac{\partial B'_x}{\partial x''} \right) - 4\pi J'_z.
\end{aligned} \tag{H.5}$$

From the temporal evolution equation of  $B'_y$ , we can see that when the initial magnetic field is  $\vec{B}(t=0) = B_0 \hat{x}$  it evolves linearly, plus fluctuations.

## H.2 Particles evolution

Deriving the definition of  $x''$  from H.1 in the limit 1D we obtain:

$$\frac{dx''}{dt''} = \frac{dx'}{dt'} - \frac{dy'}{dt'} \frac{st'}{1 + s^2 t'^2}. \quad (\text{H.6})$$

From Eq. A35 of the appendix of [43], in the limit  $Ls/c \ll 1$  (where  $L$  is the size of the simulation), we get  $dx'/dt'$  and  $dy'/dt'$ :

$$\begin{aligned} \frac{dx'}{dt'} &= u'_x \text{ and} \\ \frac{dy'}{dt'} &= u'_y + su'_x t'. \end{aligned} \quad (\text{H.7})$$

Reemplazing H.7 in H.6 we get:

$$\frac{dx''}{dt''} = \frac{u'_x}{1 + s^2 t'^2} - u'_y \frac{st'}{1 + s^2 t'^2}. \quad (\text{H.8})$$

Eq. H.8 implies that  $dx''/dt''$  is the scalar product between  $\vec{u}'$  and  $\langle \vec{B} \rangle / |\langle \vec{B} \rangle| (= (\hat{x} - st'\hat{y}) / (1 + s^2 t'^2)^{1/2})$ , corrected by the "expansion" of the 1D domain which provides the extra factor  $1/(1 + s^2 t'^2)^{1/2}$ .

In our 1D configuration, we use the same time definition ( $t'' = t'$ ) and momentum of the particles ( $\vec{p}'' = \vec{p}'$ ) used in [43]. Thus, the evolution of  $\vec{p}''$  does not change and, in the limit  $Ls/c \ll 1$ , is given by:

$$\frac{d\vec{p}''}{dt''} = q_s (\vec{E}' + \frac{\vec{u}'}{c} \times \vec{B}') + sp'_x \hat{y}, \quad (\text{H.9})$$

where  $q_s$  is the particle's electric charge and  $\vec{u}' = \vec{p}'/m\gamma'$ , with  $m$  and  $\gamma'$  being the particle's mass and Lorentz factor, respectively.